Computational Modeling of the Chlamydial Developmental Cycle Reveals a Potential Role for Asymmetric Division

Travis J. Chiarelli,[a] Nicole A. Grieshaber,[a] Cody Appa[a], Scott S. Grieshaber[a] #

[a]Department of Biological Sciences, University of Idaho, Moscow, Idaho, USA

Keywords: Chlamydia, differentiation, computational modeling

Running Title: Modeling of the Chlamydial Developmental Cycle

#Corresponding Author:

Scott S. Grieshaber

University of Idaho

Department of Biological Sciences

Moscow, ID 83844-3051

scottg@uidaho.edu

Ph: 352 575 0394

Abstract:

Chlamydia trachomatis is an obligate intracellular bacterium that progresses through an essential multi cell form developmental cycle. Infection of the host is initiated by the elementary body (EB). Once in the host, the EB cell differentiates into the non-infectious, but replication competent, reticulate body, or RB. After multiple rounds of replication, RBs undergo secondary differentiation eventually producing newly infectious EBs.

Here we generated paired cell type promoter reporter constructs and determined the kinetics of the activities of the *euo*, *hctA* and *hctB* promoters. The paired constructs revealed that the developmental cycle produces at least three phenotypically distinct cell types; the RB (*euo*prom+), IB (intermediate body, *hctA*prom+) and EB (*hctB*prom+). Additionally, results from this study showed that RBs amplify in number early in infection before reaching a plateau mid cycle. This data, along with the kinetic data from the three dual promoter constructs, was used to generate two computational agent-based models to reproduce the chlamydial developmental cycle. Both models simulated EB germination, RB amplification, IB formation and EB production but differed in the mechanism that generated the IB. The Direct Conversion and the Asymmetric Production models predicted different behaviors for the RB population which were experimentally testable. In agreement with the Asymmetric Production model, RBs acted as stem cells after the initial amplification stage, producing one IB and self-renewing after every division. Additionally, the data indicated that cell division was required for IB and EB production which supports the Asymmetric Production model over the Direct Conversion model. We also demonstrated that IBs are a transient cell population, maturing directly into EBs after formation without the need for cell division. The culmination of these results suggests that the developmental cycle can be described by a four stage model, EB germination, RB amplification/maturation, IB production, and EB formation.

Importance:

Chlamydia trachomatis is an obligate intracellular bacterial pathogen responsible for both ocular and sexually transmitted infections. All *Chlamydiae* are reliant on a complex developmental cycle, consisting of both infectious and non-infectious cell forms. The EB cell form initiates infection, whereas the RB cell replicates. The infectious cycle requires both cell types as RB replication increases the cell population while EB formation disseminates the infection to new hosts.

The mechanisms of RB to EB development are largely unknown. Here, we developed unique dual promoter reporters and used live cell imaging and confocal microscopy to visualize the cycle at the single cell and kinetic level. These data were used to develop and test two agent-based models, simulating either direct conversion of RBs to EBs or production of EBs via asymmetric RB division.

Our results suggest that RBs mature into a stem cell-like population producing intermediate cell forms through asymmetric division, followed by maturation of the intermediate cell type into the infectious EB. Ultimately a more complete mechanistic understanding of the developmental cycle will lead to novel therapeutics targeting cell type development to eliminate chlamydial dissemination.

Introduction

Chlamydiae are obligate intracellular bacterial parasites that cause an array of diseases in both humans and animals. *Chlamydia trachomatis*, a human-adapted pathogen, is the leading global cause of bactrerial sexually acquired infections and preventable blindness. In 2019, the CDC reported 1.8M *C. trachomatis* infections within the United States alone, with the most recent reports indicating that rates increased 10.0% in women and 32.1% in men from 2015-19 (1,2). This increase in infection rates has been reported across all racial/ethnic groups and affects all age groups (2).

Chlamydial growth and development has classically been characterized as a biphasic cycle, consisting of two primary cell forms: the elementary and reticulate body (3). These cell forms maintain a division of labor throughout the infectious cycle and are essential for chlamydial proliferation. The elementary body (EB) is the infectious cell form and initiates host cell invasion by pathogen-mediated endocytosis (4). The EB cell form is non-replicative and the chromosome is tightly compacted by nucleoid associated proteins (5,6). Upon entry into the host, the EB undergoes large transcriptional and phenotypic changes, maturing into the reticulate body (RB) in a process that takes up to 12 hours for serovar L2 (7,8). The RB is replication competent but non-infectious and must re-differentiate back into the EB to disseminate the infection to new host cells (9,10).

Electron micrographs have also shown the presence of a transitory cell form, termed the intermediate body (IB). IBs are present beginning between 20 and 24 hpi for serovar L2 and are characterized by a semi-condensed nucleoid similar to the EB, but are significantly larger giving them a target-like appearance (8,11). Due to the presence of the IB and its appearance as a transitory form, it is currently hypothesized that a subset of RBs undergo large morphological changes to convert directly into EBs.

We previously reported the development of a live-cell reporter system to follow the chlamydial cycle in real time at the single inclusion level. A number of different gene promoters were designed to drive the expression of fluorescent proteins in order to follow RB growth and EB development. These

kinetic data suggested that the promoters fell into three temporal categories exemplified by the activity of the *euo* (early), *hctA* (mid) *and hctB* (late) promoters (11).

In this study, paired promoter reporter constructs were developed to determine the temporal and spatial relationships between the activities of the *euo*, *hctA* and *hctB* promoters at the kinetic and single cell level. Based on the expression kinetics of these reporters and their kinetic relationships to each other, computational agent-based models were created to best represent the developmental cycle. Two models were developed to explain the data: a RB to IB direct conversion model and an asymmetric division/production model. The outputs of simulations from these models were compared to experimental data to determine which mechanism was best supported. Our model and data suggest a novel RB amplification/maturation step where the RB initially divides symmetrically to produce two RBs and increase RB numbers, followed by maturation of the RB to an asymmetrically dividing cell that produces one IB while regenerating the RB. Our data also support the direct maturation of the IB cell type into the EB without the need for cell division.

Results:

Development of dual fluorescent cell reporter constructs to determine cell type gene expression during the developmental cycle. To visualize expression kinetics and expression relationships of cell type fluorescent reporters at the single inclusion and single cell level, three dual fluorescent developmental gene expression reporter strains, *hctA*prom-*euo*prom, *hctB*prom-*hct*Aprom, and *hctB*prom-*euo*prom were created. For the *hctA*prom-*euo*prom (AMELVA) construct, the *euo* promoter was used to drive the expression of the green fluorescent protein variant, mNeonGreen (mNG) (12) fused in frame to the LVA protein degradation tag which reduced the fluorescent half-life to ~30 min (13), and the *hctA* promoter was used to drive the expression of the red fluorescent protein mKate2 (14) (Fig. S1A). The *hctB*prom-*euo*prom (BMELVA) dual reporter construct was created by replacing *hctA* prom in AMELVA with *hctB*prom to drive mKate2 expression (Fig. S1B). Lastly, to create the *hctB*prom-*hctA*prom (BMALVA) dual reporter, the *hctA* promoter was used to drive mNG(LVA) and the *hctB* promoter was

used to drive mKate2 expression (Fig. S1C). Each construct was transformed into *Chlamydia trachomatis* L2, creating the L2-AMELVA, L2-BMELVA, and L2-BMALVA reporter strains.

Host cells were infected with each strain for 30 hours followed by fixation. Confocal microscopy revealed that the three promoters were active exclusively from each other (Fig. 1A). The *euo*prom(LVA) signal from the L2-AMELVA strain was present in large RB sized cells, while *hctA*prom was active in a subset of large and small cells but in a population distinct from *euo*prom+ cells (Fig. 1A, L2-AMELVA). The *euo*prom(LVA) signal from L2-BMELVA was also present in large cells only, while the *hctB*prom signal was present in small cells and in an entirely distinct population (Fig. 1A: BMELVA). In the L2-BMALVA infected cells, *hctA*prom expression was visible in large and small cells while *hctB*prom signal was detected in small cells. Again, the two promoters were active in distinct, non-overlapping populations (Fig. 1A: L2-BMALVA).

The kinetics of each promoter was determined at the single inclusion level using live-cell microscopy. Host cells were infected with each strain and imaged for both GFP and RFP from 10 hpi until 50 hpi at 30 minute intervals. *Euo*prom(LVA) signal from L2-AMELVA was first detected at ~14 hpi and increased exponentially until ~26 hpi after which time the signal reached a plateau that was maintained for the duration of the infection (Fig. 1B, L2-AMELVA). The *hctA*prom(mKate2) signal was first detectable at ~18 hpi with an exponential increase in expression until 28 hpi, followed by a linear increase until the end of the experiment (Fig. 1B, L2-AMELVA). Like L2-AMELVA, the *euo*prom(LVA) signal for L2-BMELVA followed the same kinetics with an early exponential increase followed by a signal plateau (Fig. 1B, L2-BMELVA). The *hctB*prom signal in these inclusions became detectable at ~24 hpi and increased exponentially until ~34 hpi. After this brief exponential phase, *hctB*prom(mKate2) signal increased at a linear rate until the end of the experiment (Fig. 1B, L2-BMELVA). Live-cell kinetics of L2-BMALVA showed that *hctA*prom(LVA) activity initiated around 18 hpi, however expression approached steady state kinetics and did not accumulate (Fig. 1B: L2-BMALVA). *hctB*prom(mKate2) demonstrated the same kinetics as for the L2-BMELVA strain (Fig. 1B). The short half-life of the LVA tagged mNG allowed for spatial and kinetic resolution of three cell types. The observation that *hctA*prom was temporarily active after *euo*prom

and before *hctB*prom, and the observation that *hctA*prom is active in a distinct cell population from *euo*prom+ cells and *hctB*prom+ cells suggest that *hctA*prom is active in the IB cell population. Overall, these data suggest that the developmental cycle can be represented by three phenotypically distinct cell types; RB cells (*euo*prom+), IB cells (*hctA*prom+) and EB cells (*hctB*prom+).

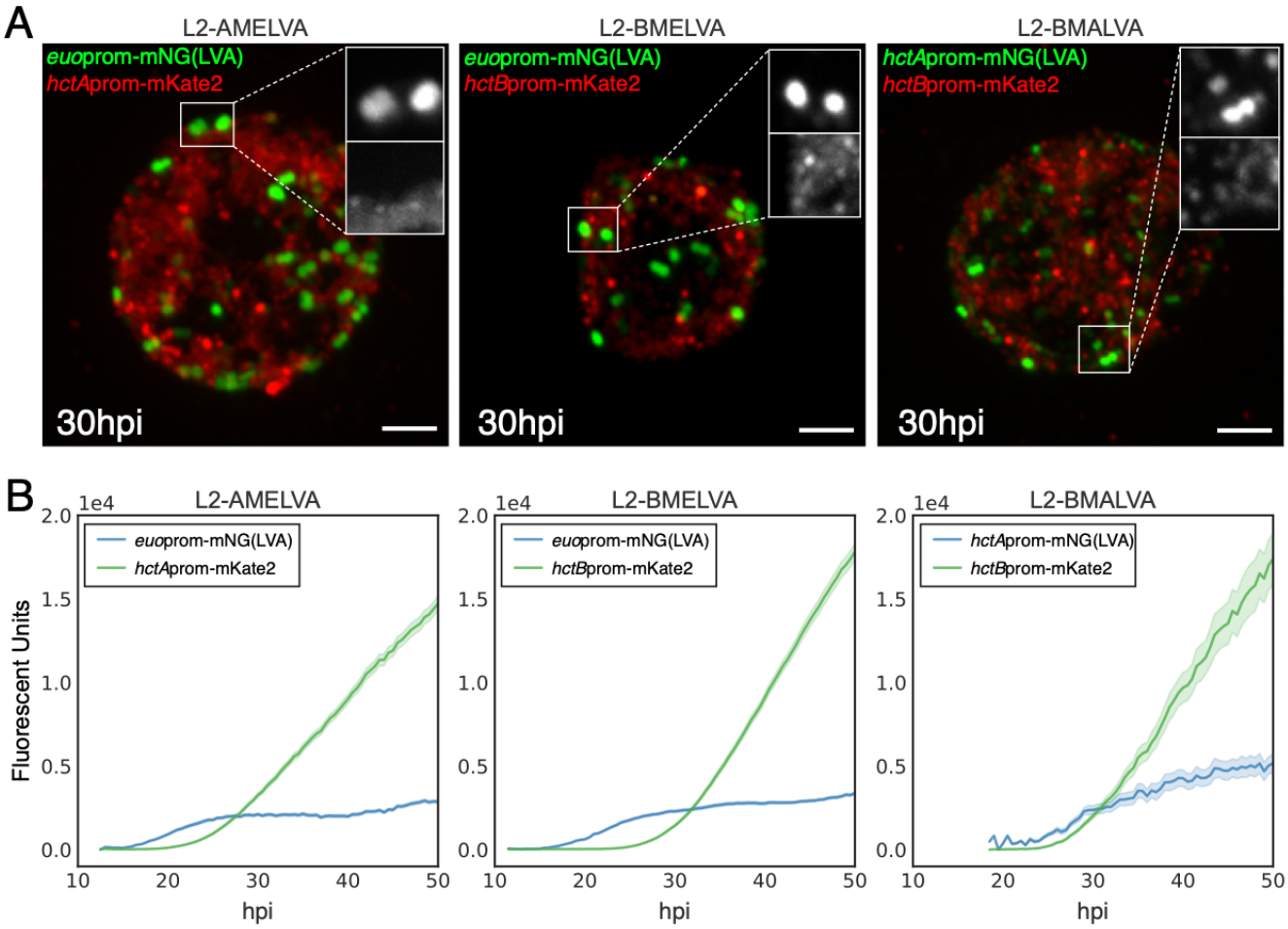

Figure 1: Dual cell-form specific promoter reporter chlamydial strains. A. Representative confocal micrographs of Cos-7 cells infected with *Ctr*-L2-*hctA*prom-mKate2_*euo*prom-mNG(LVA) (L2-AMELVA), *Ctr*-L2-*hctB*prom-mKate2_*euo*prom-mNG(LVA) (L2-BMELVA) and *Ctr*-L2-*hctB*prom-mKate2_*hctA*prom-mNG(LVA) (L2-BMALVA) reporter strains at 30 hpi. Magnified FOVs demonstrate cell-form specific expression in individual cells (mNG(LVA): top, mKate2: bottom). Scale bar = 10 µm. **B.** Live-cell expression kinetics of the three dual promoter reporter strains from >50 individual inclusions. Infections were monitored from 10-50 hpi via automated live-cell fluorescence microscopy. Average intensities are shown, cloud represents SEM.

In addition to population level kinetics, live-cell imaging revealed the interrelated kinetics of the activity of these promoters. The kinetic data from individual inclusions of both L2-AMELVA (Fig. 2A) and L2-BMELVA (Fig. 2B) revealed that there was significant heterogeneity in the maximal expression level of the *euo*prom plateau. Interestingly, the variation in *euo*prom expression from the paired expression constructs correlated with the rates of *hctA*prom (L2-AMELVA) and *hctB*prom (L2-BMELVA) signal accumulation, i.e. inclusions exhibiting high *euo*prom plateaus had steeper slopes for *hctA*prom and *hctB*prom signal accumulation, while lower *euo*prom signal correlated with a lower rate of *hctA*prom and *hctB*prom signal accumulation (Fig. 2A and B). When the *hctA*prom and *hctB*prom signals were normalized to the *euo*prom signal plateau for each inclusion, the variation in the slopes of *hctA*prom(mKate2) and *hctB*prom(mKate2) accumulation was dramatically reduced (Fig. 2A and B). This variability in the maximum expression levels of *euo*prom suggested that each inclusion contained differing numbers of RB (*euo*prom+) cells during the plateau phase, which in turn lead to the varying IB (*hctA*prom) and EB (*hctB*prom) accumulation rates.

To test whether the differing plateau signal of *euo*prom expression was due to differing RB numbers, cells were infected with L2-BMELVA at an MOI of ~0.1 and fixed and stained with DAPI every 2 hours from 14 to 48 hpi. Infected cells were imaged by confocal microscopy and cell type quantification was carried out using an automated cell counting workflow using the open-source software FIJI and the TrackMate plugin to count individual *Chlamydia* based on fluorescent reporter intensity (15). These experiments revealed that RB (*euo*prom+) cells increased in number from 14 hpi until 26 hpi, reaching an average of ~30/inclusion (Fig. 2C). After this time point, the average number of RBs was unchanged. However, it was clear that the maximum number of RBs in each inclusion varied significantly with some inclusions having as few as one *euo*prom+ cell while others had as many as 59 RBs/inclusion during this plateau phase (26-48hpi) (Fig. 2C). A similar time course was carried out for cells infected with L2-BMALVA, with similar results. IBs (*hctA*prom+) cells increased in number from 18 hpi until reaching a maximum at 32 hpi, after which the average of IBs/inclusion remained steady (Fig. 2D). Again, similar to

the *euo*prom+ cells, the number of *hctA*prom+ cells was significantly different on a per inclusion basis with some inclusions having as few as a single *hctA*prom+ cell while others had as many as 65 during the plateau phase (Fig. 2D). These data suggest that the chlamydial developmental cycle produces significant heterogeneity between inclusions, but that despite this heterogeneity, each inclusion produces similar kinetic relationships between cell types.

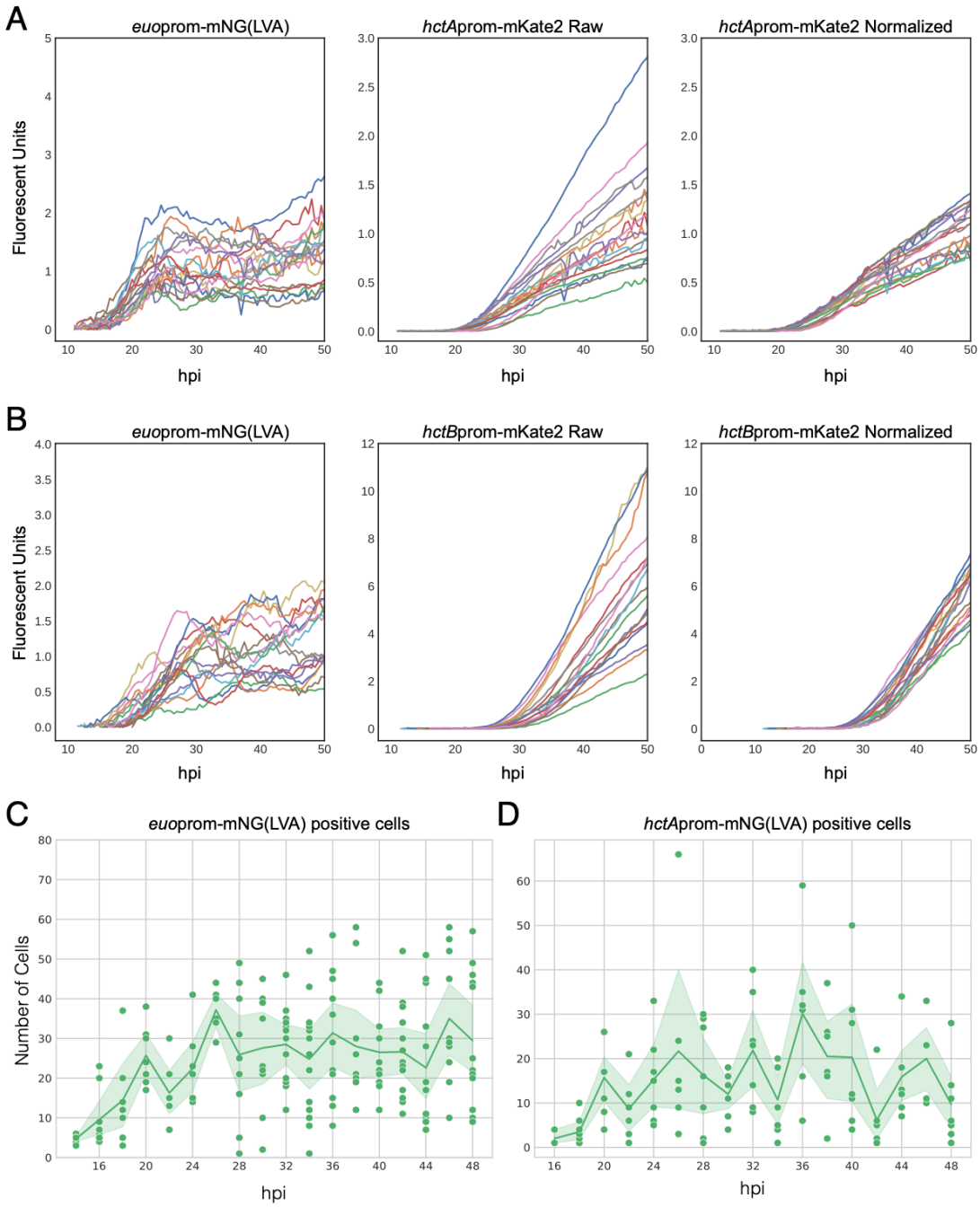

Figure 2: IB and EB production is dependent on the number of RBs. Cos-7 cells were infected with purified *Ctr*-L2-prom EBs. **A.** Live-cell expression kinetics from single inclusions from L2-AMELVA infected cells. Graphs show *euo*prom-mNG(LVA) expression, *hctA*prom-mKate2 expression, and *hctA*prom-mKate2 expression normalized to the paired average expression levels of *euo*prom-mNG(LVA) between 30-38 hpi. **B.** Live-cell expression kinetics from single inclusions of L2-BMELVA infected cells. Graphs show *euo*prom-mNG(LVA) expression, *hctA*prom-mKate2 expression, and *hctB*prom-mKate2 expression normalized to the paired average expression levels of *euo*prom-mNG(LVA) between 30-38 hpi. **C and D.** Quantification of *euo*prom+ or *hctA*prom+ cell counts within individual inclusions from fixed samples. Infections were fixed every two hours from 14-48 hpi and stained with DAPI. Inclusions were imaged by confocal microscopy for DAPI, GFP and RFP. Individual dots represent the number of promoter reporter+ chlamydial cells within individual inclusions. Solid line represents the mean number of promoter reporter+ cells per time point. Sample size ranged between 3-14 inclusions dependent on the time point. Cloud represents 95% ci.

Modeling the chlamydial developmental cycle. Dissecting the mechanisms that control the developmental cycle in *Chlamydia* has in part been inhibited by the reliance on population based studies. Using the individual inclusion kinetic data and individual cell expression data generated from L2-AMELVA, L2-BMELVA and L2-BMALVA, we divided the cycle into discrete steps: EB germination, RB amplification, IB formation, and EB maturation. To explore potential mechanisms involved in these steps, two agent based models (ABMs) were developed to describe the developmental cycle using the Python-based bacterial growth simulation platform, Cellmodeller (16). Euo, HctA and HctB protein expression was simulated in each cell type over time for both models (Sup model). Additionally, germination was set at 10 hpi as the first replication event has been previously reported at this time point (11,17), and agrees well with initiation of *euo* promoter expression (Fig. 1 and 2) (11). The two models differed in the mechanism controlling RB amplification and IB formation. The Asymmetric Production model used a RB maturation mechanism where early RBs (designated the RB_R) replicate to produce two identical RB_R daughter cells, resulting in RB_R number amplification. This step is followed by a RB_R maturation phase where the RB_R matures over time into a cell form that undergoes asymmetric cell division (designated the RB_E), producing one RB_E daughter cell and one IB daughter cell. The Direct Conversion model used a stochastic direct conversion mechanism where early RBs replicate resulting in RB number amplification followed by an increase in the chance that an RB transitions into the IB state. This stochastic chance of conversion increases over time before reaching a maintenance state where RB amplification and

conversion rates are matched (Sup model). Both models reproduced the developmental kinetics that were observed using L2-AMELVA, L2-BMELVA and L2-BMALVA (Fig. 3A and Fig. 1 and 2). However, the stochastic model needed to be constrained to match the experimental data. When conversion became greater than RB replication, RB numbers dropped to extinction. Conversely, when the RB replication rate remained higher than the conversion rate, RBs quickly outnumbered EBs (Fig. 3B).

Although both models could produce similar kinetics at the population level, simulations of individual inclusions demonstrated large kinetic differences. For the Asymmetric Production model, simulated inclusions with high RB numbers had corresponding high EB production rates, while inclusions with low RB numbers had corresponding low EB production rates. The EB production rate for each inclusion, regardless of RB numbers, was linear while the RB population numbers remained unchanged over time (Fig. 3C: Asymmetric Production). The kinetics for the Direct Conversion model had similar trends, however there were obvious runs of over and under amplification/conversion for both RB and EB numbers in the individual inclusion simulations, demonstrating that the stochastic mechanism can reliably reproduce the observed data only on the population level. These simulations suggest that the Asymmetric Production model is a better match for the observed developmental kinetics.

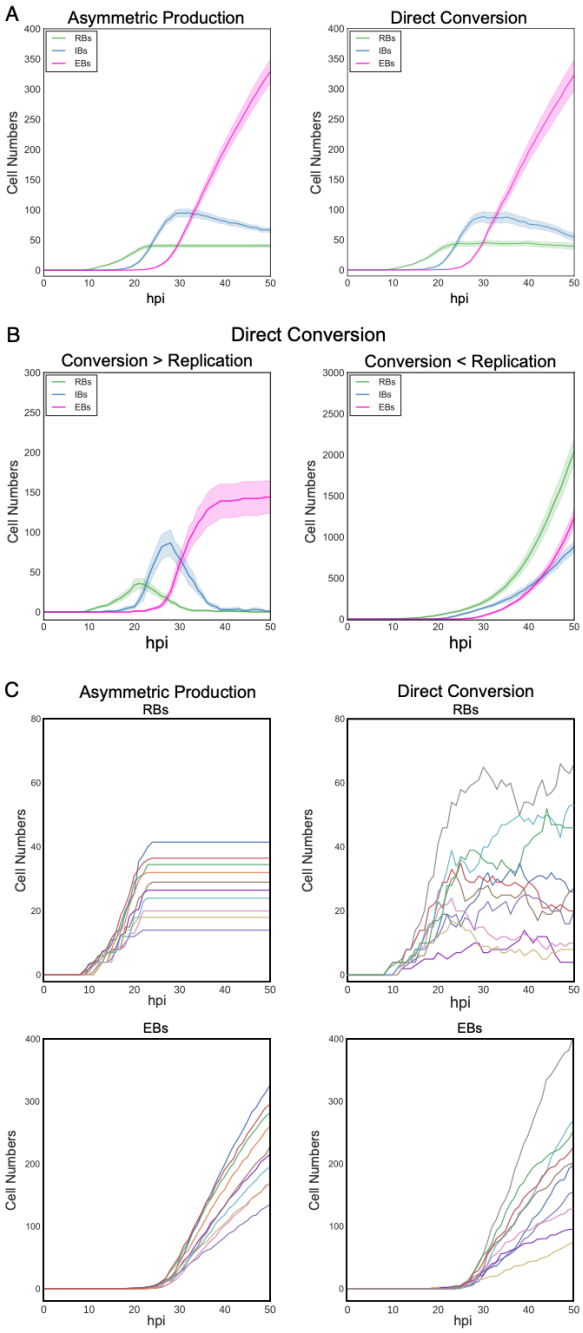

Figure 3: Simulations of inclusion kinetics from the Asymmetric Production and Direct Conversion models. A. Simulated developmental kinetics of the Asymmetric Production and Direct Conversion models. RBs: green, IBs: blue, and EBs: pink. **B.** Simulated kinetics of the direct conversion model if conversion outcompetes replication (Panel 1) or replication outcompetes conversion (Panel 2). RBs: green, IBs: blue, and EBs: pink. **C.** Individual traces of simulated RB and EB kinetics on a per-inclusion level for the Asymmetric Production and Direct Conversion models. Colors of individual inclusion traces are paired between the RB and EB cell forms per model simulation. Infections were simulated from 0-50 hpi. For **A and B,** the average of 20 simulations/model are shown, cloud represents SEM. Model parameters can be found in **Supplemental Materials**.

Steady state vs stem cell population. The Asymmetric model predicts that after amplification the RBs act as a stem cell population, producing IBs while self-renewing after every division (Mov. S1). In contrast, the Direct Conversion model predicts that RBs convert directly into IBs and are subsequently replaced by a dividing RB population, producing a steady state of RBs (Mov. S2). To determine which of these phenotypes the RB is exhibiting, live-cell imaging at high resolution (40X objective) of cells infected with L2-BMELVA was used to follow RB behavior. Cells infected with L2-BMEVLA were imaged for *euo*prom and *hctB*prom expression every 15 minutes starting at 24 hpi until 60 hpi. We imaged from 24 hpi until 60 hpi as this covers the end of the RB amplification stage until the end of the cycle. Imaging revealed that the number of RBs (*euo*prom+) per inclusion remained roughly the same throughout the experiment (Fig. 4A and Mov. S3). The RBs in each inclusion were easily tracked from one time point to the next and did not disappear while new RBs appeared. We also observed two binary divisions (RB amplification events) occurring between 26 hpi and 31 hpi (Fig. 4A, #3a and b, #5a and b, and Mov. S3). These newly formed RBs also remained trackable within the inclusion for the remainder of the experiment. These observations are consistent with stem cell like behavior of the RBs after amplification.

Both models predicted that the IB cell type is maintained at steady state, i.e IBs mature into EBs and new IBs replace the maturing cells. To investigate the dynamics of the IB population, the L2-BMALVA strain was imaged from 24 hpi until 60 hpi at 15 min intervals. The dynamics of the IBs (*hctA*prom+ cells) resembled steady state kinetics; *hctA*prom+ cells would disappear while new *hctA*prom+ cells would appear (Fig. 4B, Mov. S4).

Together these data strongly support the Asymmetric Production model that predicts that RB numbers are amplified between 12 hpi and 28 hpi followed by a stem cell like behavior, producing one

IB at division. In contrast, the IBs behave as a steady state population where, once formed, the IBs are converted directly into EBs.

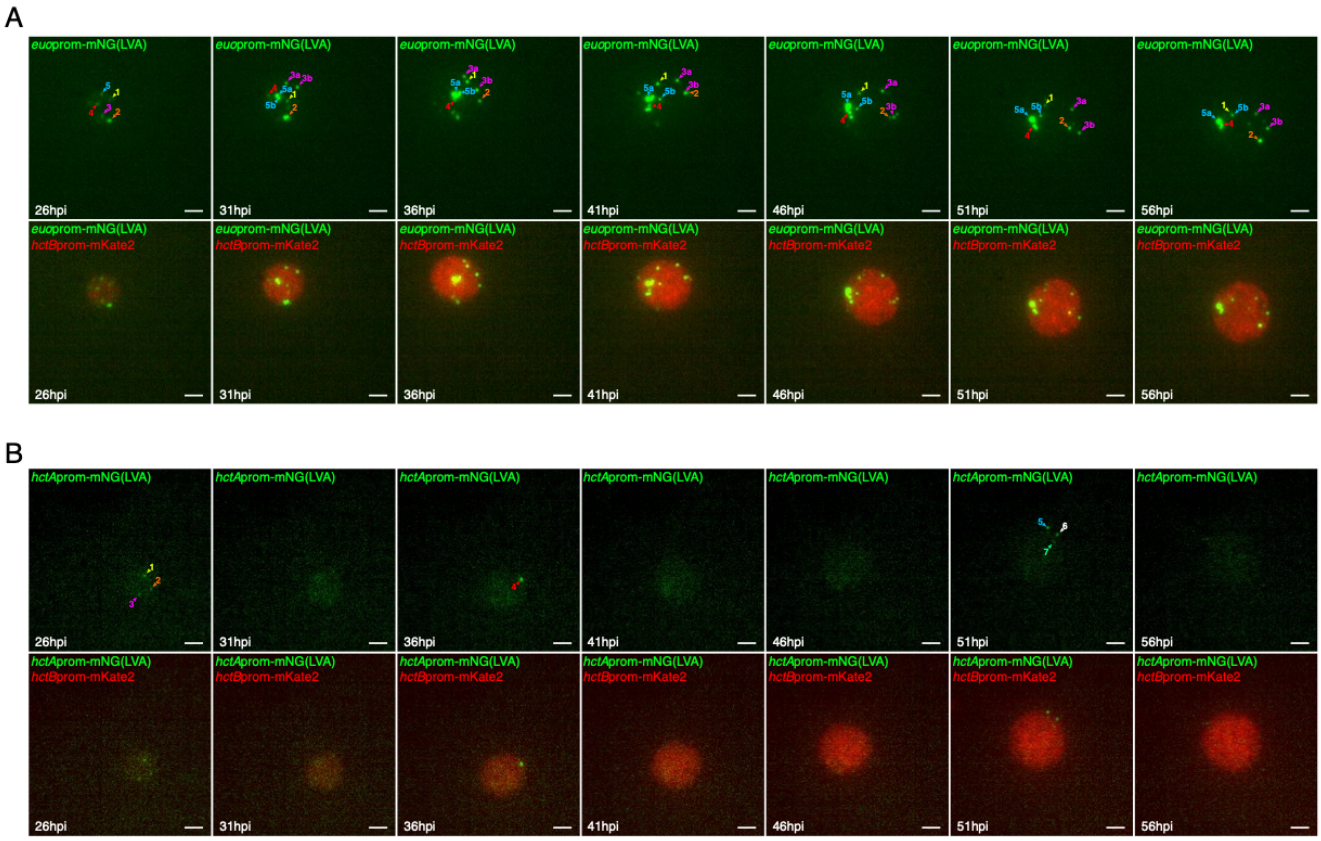

Figure 4: RBs persist as a stem cell population while IBs are at steady state. Cos-7 cells were infected with either (**A**) L2-BMELVA (RB/EB) or (**B**) L2-BMALVA (IB/EB). Individual inclusions were imaged using a 40X objective every 15 min from 24-60 hpi. Numbered arrowheads indicate individual *euo*prom-mNG(LVA)+ (RB) or *hctA*prom-mNG(LVA)+ (IB) cells through time. (**A**) Two binary division events occurred between 26 to 31 hpi, corresponding to cells 3a/b and 5a/b. Scale bar = 10 μm. The 15 min interval time lapse videos for each inclusion can be found in supplemental material (**Mov. S3** and **S4)**.

The role of cell division on the RB population. Simulations of the two competing ABMs predicted different developmental outcomes if cell division was inhibited. The Asymmetric model predicted that RBs produce IBs only at division. Therefore, an immediate block in the formation of new IBs would occur but RB numbers would remain unaffected if replication was inhibited at 30 hpi (Fig. 5A). In contrast, the Direct Conversion model predicted that RB numbers would drop overtime if cell division was inhibited at 30 hpi, eventually disappearing as the RBs converted into IBs but were not replaced by further RB replication

(Fig. 5B). To test these predictions experimentally, two cell replication inhibitors were used, penicillin (Pen) and ciprofloxacin (Cip). *Chlamydia* does not contain a peptidoglycan cell wall and instead uses peptidoglycan in septum formation, therefore Pen treatment of *Chlamydia* inhibits cell division (18). Ciprofloxacin prevents bacterial DNA replication by inhibiting topoisomerases and DNA-gyrase (19). Cells were infected with L2-BMELVA and >20 inclusions per treatment were imaged using a 60X 1.4 NA objective. Individual inclusions were imaged at multiple z planes to visualize and quantify all the RBs in the inclusion. Images were collected from the live cultures at antibiotic treatment (30 hpi) and 10 hours later (40 hpi) (Fig. 5C and D). The number of *euo*prom+ cells (RBs) was quantified on a per-inclusion basis. The same inclusions were quantified at each time point. Consistent with the confocal time-series experiment, there was a large variation in the number of RBs in individual inclusions, ranging from a single RB to greater than 50 RBs (Fig. 5C). However the number of RBs per inclusion remained essentially constant between the 30 hpi and 40 hpi timepoints (Fig. 5C). The mean ratio of RBs at 30 hpi and 40 hpi per inclusion was 1.27±0.28 for untreated, 1.18±0.24 for Pen treated and 1.51±0.35 for Cip treated (Fig. 5D). There was an increase in RB numbers in each inclusion when treated with Cip, but never more than double. We speculate that although Cip treatment inhibited initiation of DNA replication, it did not significantly impact the continuation of DNA replication and allowed cell division to finish in RBs that had already initiated DNA synthesis. This is in agreement with our published data demonstrating that RBs are undergoing continuous DNA replication as indicated by a replication index of 1.5 (20). This index is a ratio of sequencing coverage near the origin of replication vs coverage near the terminus and represents the growth rate of the population. An RB replication index of 1.5 demonstrates the presence of partially replicated chromosomes (20).

To confirm that chlamydial DNA replication was inhibited by Cip, digital droplet (ddPCR) was performed on L2-BMELVA infected samples treated with either Cip, Pen, or mock at 30 hpi. Host monolayers were harvested every 4 h from 26-54 hpi. As previously reported, genome copy number continued to increase in the Pen treated samples (11,21). There was however, a large reduction in

genome copy accumulation after Cip treatment when compared to the mock and Pen treated samples (Fig. S2).

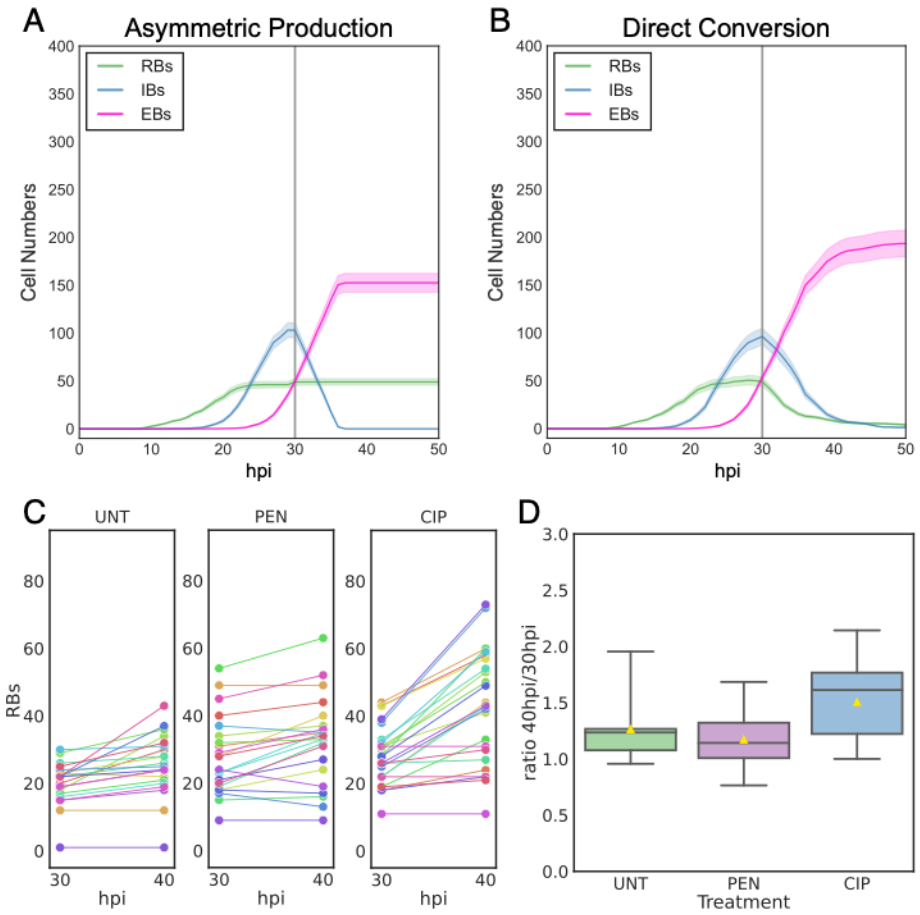

Figure 5: RBs do not convert into IBs after cell division inhibition. Simulated cell-form kinetic of cell division inhibition in the Asymmetric Production (**A**) and Direct Conversion model (**B**). RBs: green, IBs: blue, and EBs: pink. Infections were simulated from 0-50 hpi. Gray vertical line indicates time of simulated cell-division inhibition (30 hpi). Average cell form subpopulation numbers of 20 simulations per model are shown, cloud represents SEM. **C.** Cos-7 cells were infected with purified L2-BMELVA EBs. Infected cells were treated at 30 hpi with either vehicle (UNT), penicillin-G (PEN) or ciprofloxacin (CIP). The number of *euo*prom-mNG(LVA)+ cells were counted per inclusion at 30 and 40 hpi. Horizontal lines connect the same imaged inclusions. **D.** Boxplot demonstrating the 40/30 hpi ratio of RBs per treatment. The center gray line represents the median number of RBs, the yellow triangle represents the mean.

The role of cell division on the IB population and EB production. Simulations of the two competing ABMs also predicted different developmental outcomes in the IB population if cell division was inhibited or if RBs were eliminated at 30 hpi. The Asymmetric model produces IBs only at division, therefore blocking cell division at 30 hpi predicted an immediate block in the formation of new IBs leading to an

immediate halt in the increase in IB gene expression (Fig. 6A, Asymmetric Production). Additionally, if RBs were eliminated in the Asymmetric model, simulations again predicted that IB gene expression would halt immediately, and the kinetics would match that of the cell division inhibitors (Fig. 6A). In contrast, after replication was inhibited, the Direct Conversion model predicted that IB gene expression would continue to increase over a 12 hour period as the RBs converted into IBs, at which point IB gene expression would halt as IBs could not be replenished by RB cell division (Fig. 6A, Direct Conversion). Simulation of RB elimination in the Direct Conversion model resulted in an immediate halt in IB gene expression, kinetics which differ significantly from those of cell division inhibition (Fig. 6A, Direct Conversion).

To test these predictions experimentally, cell replication was inhibited with Pen and Cip and RBs were eliminated by overexpression of FtsI. Ectopically expressed FtsI in *Chlamydia* results in the death of dividing cells as the fission plane is mislocalized. The ORF of *ftsI* was cloned in frame with a C-terminal 3XFLAG epitope into our translational control system using the previously published E-riboswitch expression plasmid (13). The *euo*prom-mNG(LVA)_*hctB*prom-mKate2 promoter reporter cassette was cloned into the E-*ftsI*3XFLAG vector and transformed into *Chlamydia trachomatis* L2 creating the strain L2-E-*ftsI*-BMELVA. Elimination of the RB population by induction of FtsI3XFLAG was confirmed by immunofluorescence confocal imaging and by assessing DNA replication. Induction of FtsI with theophylline (Tph) at 20 hpi resulted in the loss of gene expression from both promoters by 30 hpi (Fig. S3A). DNA replication was also halted as assayed by ddPCR (Fig. S3B). An additional dual promoter reporter strain was created using *hctA*prom-mEos3.2 paired with *hctB*prom-mKate2 (L2-BMAMEO). The mEos3.2 GFP variant was used as it does not have the LVA degradation tag and therefore allowed us to quantify IB production as it accumulates over time. This dual color promoter reporter cassette was also cloned into the E-*ftsI*3XFLAG plasmid and transformed into *Chlamydia*, creating L2-E-*ftsI*-BMAMEO.

Cells were infected with L2-BMAMEO or L2-E-*ftsI*-BMAMEO and imaged from 10 hpi until 50 hpi (Fig. 6A, Experimental Data). Pen and Cip were added at 30 hpi to the L2-BMAMEO cultures and FtsI was induced by adding Tph at 30 hpi to the L2-E-*ftsI*-BMAMEO infected cells. Live cell imaging of the

*hctA*prom-mEos3.2 produced kinetics consistent with the Asymmetric model simulations. The increase of IB production signal from *hctA*prom was almost immediately inhibited by all three treatments (Fig. 6A, Experimental Data). As we have previously documented, the *hctA*prom reactivated in the Pen treated aberrant cells after about an ~8 hour delay.

The two models also predicted differences in EB production when cell division was inhibited or RBs were eliminated. The Asymmetric Production model predicted that EB production would halt ~6 hours after all treatments indicated (Fig. 6B, Asymmetric Production). The stochastic Direct Conversion model simulations predicted that inhibition of cell division would result in a slowing followed by a halt in EB production ~18 hour post treatment, while RB elimination would result in EB production halting at ~6 hours after treatment (Fig. 6B, Direct Conversion). To directly test these predictions, EBs were collected every 4 hours from 10 to 50 hpi and used to infect fresh host cells for EB quantification. EB production was inhibited ~8 hours post cell division inhibition and FtsI induction (Fig. 6B, Experimental Data). These data taken together all support an asymmetric IB production model and not stochastic direct conversion of an RB to an IB.

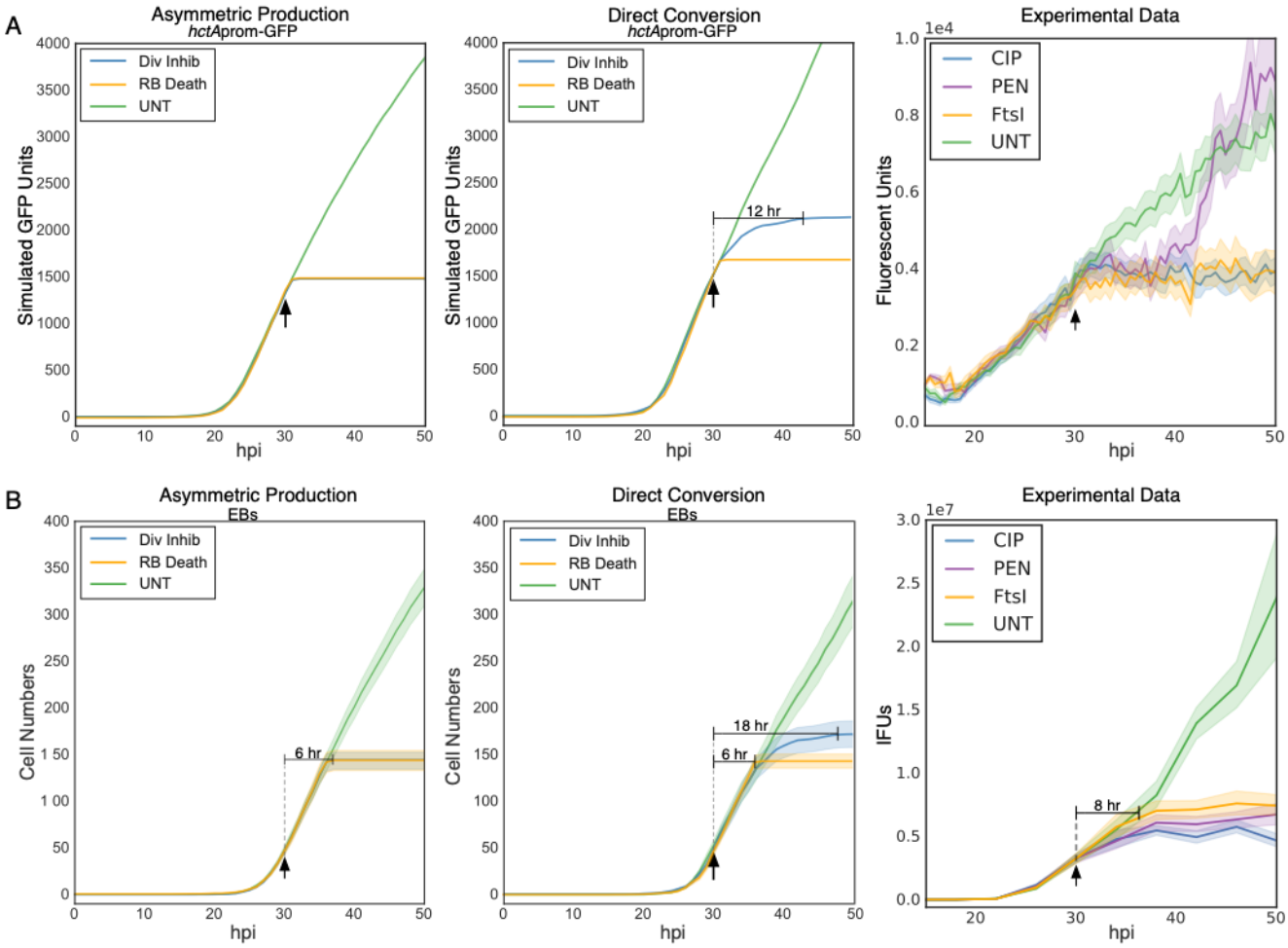

Figure 6: IB and EB production halt after cell division inhibition. A. Simulated kinetic outputs of the total accumulation of GFP from the IB-associated promoter *hctA*prom for both the Asymmetric Production and Direct Conversion models. **B.** Simulated total total EB cell numbers for both the Asymmetric Production and Direct Conversion models. Untreated: green, cell-division inhibition: blue, RB elimination: orange. Infections were simulated from 0-50 hpi. Average of 20 simulations per model are shown. **A and B, Experimental data.** Cos-7 cells were infected with L2-*ftsI*/3XFLAG-BMAMEO. Infected cells were treated at 30 hpi with vehicle (UNT): green, penicillin-G (PEN): purple, ciprofloxacin (CIP): blue, or induced for FtsI: orange. **A, Experimental Data.** Mean expression kinetics of *hctA*prom-mEos3.2. **B, Experimental data.** Mean number of infectious progeny. Arrow indicates time of treatment (30 hpi). Horizontal solid line indicates the time to inhibition of IB or EB formation. Cloud for simulations and fluorescent reporters represents SEM. IFU cloud represents 95% ci.

EB formation is independent of continued IB production. Both of our ABMs rely on the direct conversion of IBs into EBs without replication. To test this assumption, we infected cells with L2-BMELVA and used confocal imaging to assay for the expression of the EB associated promoter, *hctB*prom. Cells were infected with L2-BMELVA and replication was inhibited by treatment with Pen or Cip at 20 hpi. Untreated and treated samples were fixed and stained for DNA (DAPI) at 20 hpi and 30 hpi and imaged for DAPI, GFP and RFP fluorescence. Before treatment (20 hpi), all inclusions had *euo*prom+ cells, a large number of DAPI only positive cells, and no *hctB*prom+ cells (Fig. 7A, S4A). At 30 hpi the untreated inclusions contained *euo*prom+ cells, DAPI only cells, and *hctB*prom+ cells (Fig. 7B, S4A). The inclusions treated with Cip for 10 hours contained *euo*prom+ cells and *hct*Bprom+ cells but less DAPI only cells compared to untreated (Fig. 7B, S4B). Pen treated inclusions contained large aberrant *euo*prom+ cells, small *hctB*prom+ cells and fewer DAPI only cells at 30 hpi (Fig. 7B, S4C).

We also asked whether the elimination of the dividing cell population through FtsI ectopic expression affected IB to EB formation. Cells were infected with L2-E-*ftsI*-BMELVA and induced for FtsI expression at 20 hpi. The infected cells were fixed and stained with DAPI and confocal images were taken for DAPI, GFP, and RFP signals at 20 and 30 hpi. The inclusions in the L2-E-*ftsI*-BMELVA infected cells at 20 hpi contained *euo*prom+ cells and DAPI only stained cells, and little to no *hctB*prom+ cells (Fig. S4D, Fig. S5A). The uninduced L2-E-*ftsI*-BMELVA inclusions at 30 hpi contained *euo*prom+ cells, DAPI only positive cells, and a significant number of *hctB*prom+ cells (Fig. S5B). However, the Tph induced L2-E-*ftsI*-BMELVA inclusions at 30 hpi had misshapen cells with just a trace of *euo*prom+ signal, fewer DAPI positive cells, and a significant number of *hctB*prom+ cells (Fig. 7B, S4D). Taken together these data support the hypothesis that the IB matures directly into the EB cell form without undergoing cell division.

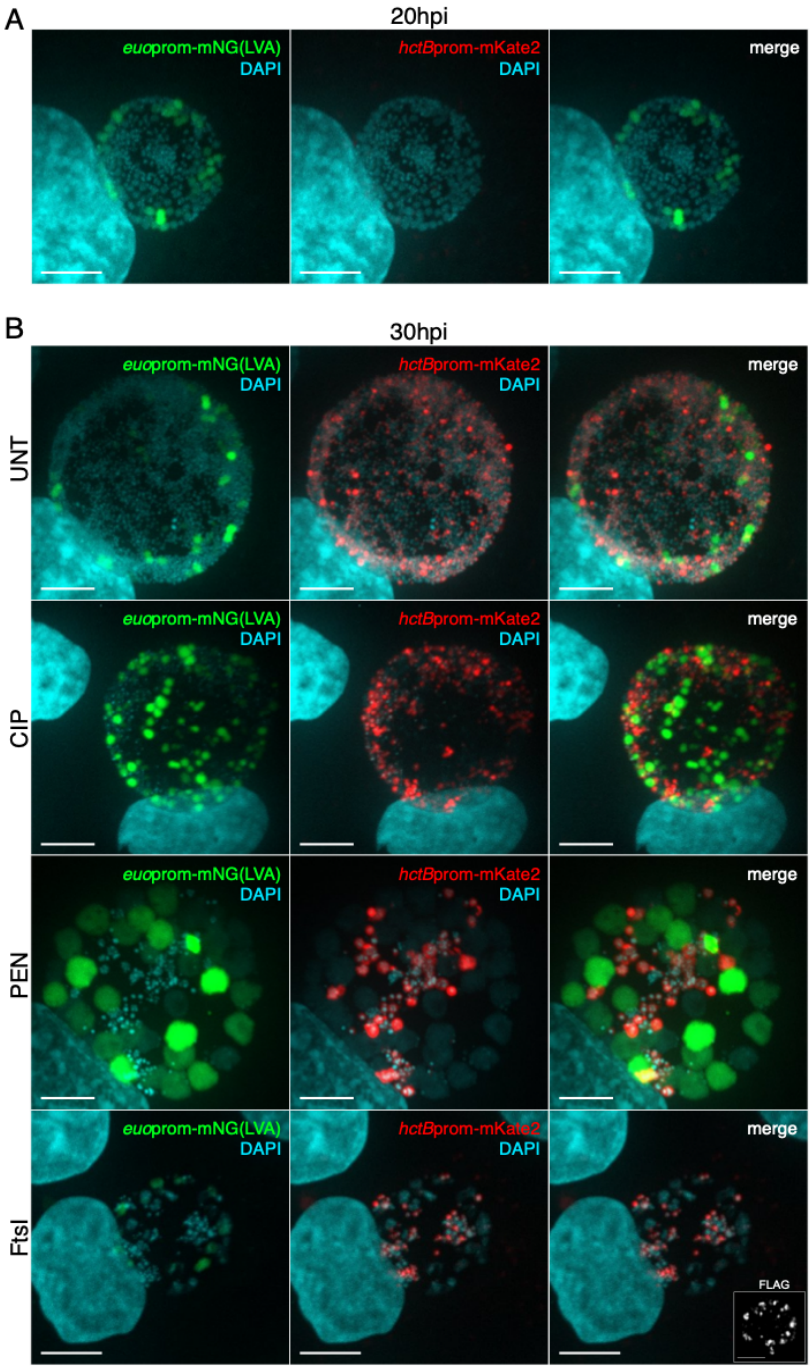

Figure 7: IB to EB development is replication independent. Cos-7 cells were infected with either purified L2-BMELVA or L2-E-*ftsI*3XFLAG-BMELVA. L2-BMELVA infected cells were treated with either vehicle (UNT), ciprofloxacin (CIP), or penicillin-G (PEN) and L2-E-*ftsI*3XFLAG-BMELVA infected cells were induced for FtsI at 20 hpi. Samples were fixed at 20 hpi (pre-treatment) or 30 hpi, and stained with DAPI. Images are z projected confocal micrographs showing *euo*prom-mNG(LVA): green, *hctB*prom-mKate2: red, and DAPI: cyan. **A.** Representative confocal micrograph of a 20 hpi. **B.** Representative confocal micrographs of 30 hpi UNT, CIP, PEN and FtsI-induced infections. Insert demonstrates positive anti-FLAG staining in the FtsI-induced sample. Scale bar = 10 μm. See **Fig. S5** for the uninduced FtsI sample).

IBs convert directly to EBs. To verify that the IB directly matures into the RB without cell division, cells were infected with L2-BMAMEO to visualize the *hctA*prom+ and *hctB*prom+ cells, and cell division was inhibited with Cip at 18 hpi. Infected cells were then fixed and stained with DAPI at 22 hpi and 34 hpi. The inclusions were imaged for DNA (DAPI), GFP (*hctA*prom) and RFP (*hctB*prom) (Fig. 8A and B). The expression levels of GFP and RFP were determined for individual chlamydial cells in three representative inclusions by identifying cells using the DAPI channel and measuring expression levels using the trackMate plugin in FIJI (Fig. 8A and B). Confocal microscopy of untreated cells at 22 hpi revealed that there were a significant number of DAPI only and *hctA*prom+ cells with very few *hctA*prom+/*hctB*prom+ cells or *hctB*prom+ only cells (Fig. 8A, UNT). At 34 hpi there were again populations of DAPI only and *hctA*prom+ cells, however many of the *hctA*prom+ cells were also positive for *hctB*prom (Fig. 8B, UNT). Similar trends were seen when cell division was inhibited by the addition of Cip at 18 hpi. The chlamydial population at 22 hpi consisted of primarily DAPI only and *hctA*prom+ cells (Fig. 8A, CIP), while many of the *hctA*prom+ cells were also *hctB*prom+ by 34 hpi (Fig. 8B, CIP). This increase in the number of double positive cells in cell division inhibited *Chlamydia* suggests that the *hctA*prom+ cells were activating *hctB*prom over time.

We also asked whether the IB could directly become an EB after the elimination of the dividing cell population by ectopic expression of FtsI. Cells were infected with L2-E-*ftsI*-BMAMEO and FtsI expression was induced at 18 hpi. At 22 hpi, there were a large number of DAPI only and *hctA*prom+ cells in the induced population. Anti-FLAG staining revealed that many of the DAPI only cells were expressing FtsI-Flag (Fig. 8A, FtsI). The inclusions at this time point contained very few *hctB*prom+ cells. At 34 hpi, there was a significant increase in the number of *hctA*prom/*hctB*prom double positive chlamydial cells, suggesting the *hctA*prom+ cells activated *hctB*prom without cell division (Fig. 8B, FtsI). The uninduced samples showed a similar pattern. These data together demonstrate that IBs (*hctA*prom+) mature directly into EBs (*hctB*prom+) and that cell division is not required for this progression.

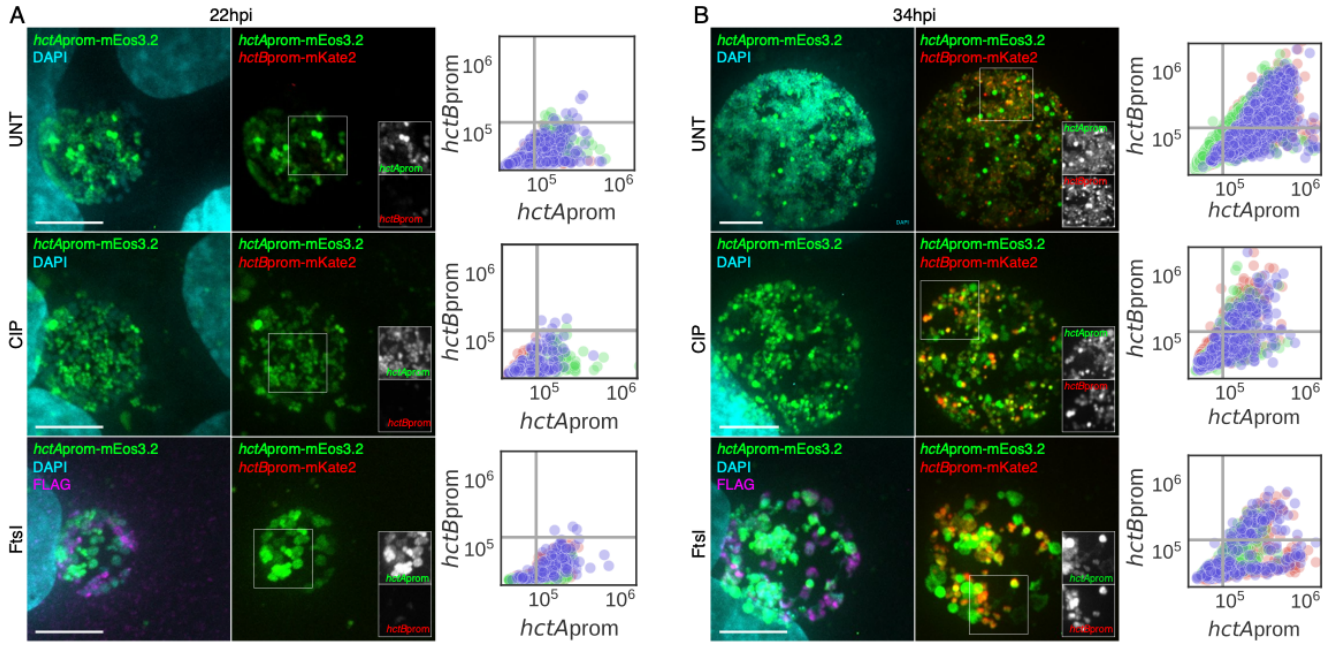

Figure 8: IBs mature directly into EBs. Cos-7 cells were infected with L2-E-*ftsI*3XFLAG-BMAMEO. Infected cells were treated at 18 hpi with either vehicle (UNT), ciprofloxacin (CIP), or induced for FtsI3XFLAG expression (FtsI). Samples were fixed at 22 hpi or 34 hpi, stained with DAPI and an anti-FLAG antibody. Images are z-projections from confocal micrographs showing *hctA*prom-mEos3.2: green, *hctB*prom-mKate2: red, DAPI: cyan, anti-FLAG: magenta. **A.** Representative confocal micrographs of 22 hpi cells along with quantification of *hctA*prom-mEos3.2 and *hctB*prom-mKate2 expression levels at the single cell level. Quantification of DAPI positive cells was performed using Trackmate from 3 individual inclusions per treatment per time point. Each color corresponds to chlamydial cells quantified within the same inclusion. **B.** Confocal micrographs of L2-E-*ftsI*3XFLAG-BMAMEO infected cells at 34 hpi either treated with vehicle (UNT), CIP, or induced to express FtsI. Inserts demonstrate the overlap of *hctA*prom-mEos3.2 and *hctB*prom-mKate2 within single cells. Quantification of DAPI positive cells was performed using Trackmate from 3 individual inclusions per treatment per time point. Each color corresponds to chlamydial cells quantified within the same inclusion. Scale bar = 10 μm.

Discussion

The developmental cycle of *Chlamydia* is central to its ability to cause disease. The cycle produces phenotypically distinct cell types with functional specificity. This includes the RB cell which replicates, leading to organism proliferation, and the EB cell type which mediates entry into new cells, disseminating the infection to new hosts. The developmental cycle has conventionally been broken down into two stages; RB replication and EB conversion. While the broad strokes of the overall cycle is described, the molecular details that regulate this process are poorly understood. Our data suggests that the current understanding of the cycle is an oversimplification. We propose that the developmental cycle

can be divided into multiple stages including: EB germination, RB amplification/maturation, IB production, and EB formation.

Our data show that the chlamydial developmental cycle produces at least three different phenotypic cell types, the RB (*euo*prom+), IB (*hctA*prom+) and EB (*hctB*prom+). The data also demonstrate that RB proliferation initiates at ~10-12 hpi and reaches a plateau by 24-26 hpi after which RB numbers remain virtually unchanged until the end of the cycle. Remarkably, at the individual inclusion level the number of RBs at plateau was highly variable with some inclusions containing a single RB while others had as many as 60. To understand the potential mechanisms that underlie these observations, we developed computational agent based models (ABMs). Two mechanistic models were developed that could recapitulate our experimental data. Both models estimate the germination time based on published time to first RB replication (17) and time to *euo*prom expression (this study). The models differ primarily in the IB production mechanism which we hypothesize is the committed step to EB formation.

Regulatory mechanisms such as RB access to or competition for inclusion membrane contact (22), reduction in RB size (8), and responses to changes in nutrient availability (23), have been proposed to explain the regulation of EB formation. Although the triggering signal for differentiation differs in these models, all propose a stochastic direct RB to EB conversion mechanism. Therefore, the Direct Conversion Model utilized a direct conversion mechanism to control RB amplification and IB production. Our second ABM, the Asymmetric Production Model, used a RB maturation/asymmetric division mechanism to control RB amplification and IB production. In this model, we proposed two RB subtypes, the RB_R which upon replication produces two identical RB_R daughter cells, and an RB_E that upon cell division produces one IB and one RB_E. The RB_R subtype matures into the RB_E subtype during the first 24 hours of infection. For both models, the IB cell exits the cell cycle and matures directly into the EB. Although both models could reproduce the measured kinetics of the developmental cycle at the population level, only the maturation/asymmetric model could reliably reproduce the observed kinetics at the single inclusion level. Even after constraining replication and conversion to avoid RB extinction or

overpopulation, the stochastic direct conversion model resulted in runs of over and under IB production that were not readily evident in the measured data.

The Asymmetric Production model predicted that the mature RB cell (RB_E) acts as a stem cell, producing one IB upon division while the other daughter cell remains an RB_E. The Direct Conversion model predicted that RB numbers are at steady state where cell division creates new RBs while other RBs convert into IBs. Using live cell microscopy, we determined that individual RBs were consistently present and trackable from time point to time point over a 30 hour time period, strongly suggesting the RB population is acting like stem cells and not a steady state population. Conversely both models predicted that the IB population is at steady state, with IBs forming and transitioning into EBs while new IBs replace those that became EBs. The behavior of individual IBs revealed by live cell imaging was consistent with a steady state population, with IBs disappearing and new ones appearing over time.

The models also predicted that inhibition of cell replication would have differing effects on the RB, IB and EB populations. The stochastic Direct Conversion model predicted that RB numbers would decline after cell division inhibition as RBs that directly converted to IBs were not replaced by new RBs through cell division. In contrast, the Asymmetric Production model predicted that inhibition of cell division would have no impact on the RB population. We found that treatment with two different cell replication inhibitors (Pen and Cip) resulted in no decrease in the RB population over a 10 hour period, again strongly supporting an asymmetric division model.

The kinetics of the IB and EB population was also predicted to differ in the two models after replication was inhibited. The Direct Conversion model predicted that inhibition of cell division would lead to a protracted inhibition of new IB formation, resulting in decreasing IB production over ~12 hours, while EB formation would also slowly decline until completely inhibited at ~18 hours after treatment. The maturation/asymmetric conversion model predicted that inhibiting cell division would inhibit new IB production nearly immediately and inhibit EB formation after the ~8 hour IB to EB maturation time (11). Live cell microscopy demonstrated that the kinetics of cell division inhibited *Chlamydia* clearly supported

the Asymmetric Production model over the Direct Conversion model as IB production halted nearly instantly and EB production halted after ~8 hours.

Both models predicted that IBs mature directly into EBs. This prediction is supported by the data showing that the IB cell type progressed to *hctB*prom expression after inhibiting cell division (Cip, Pen) or eliminating RBs through ectopic expression of FtsI. Additionally, we demonstrated that IBs mature directly from *hctA*prom single positive to *hctA*prom/*hctB*prom double positive cells after inhibiting cell division or eliminating RBs.

Overall, the data support a developmental cycle that includes an asymmetrically dividing RB population. Asymmetry has been documented for both the EB and RB cell (24–27). In addition, it has been shown that the division plane can form asymmetrically during RB division (24,28). Asymmetric cell division is a common mechanism to generate phenotypically distinct cell populations in bacteria. Many of these systems have evolved to create two cell populations; one cell acts as the stem cell while the other cell disseminates the bacterial colony to new environments. Both *Caulobacter crescentus* and some members of *Chlamydia's* nearest phylogenetic neighbors, the *Planctomycetes,* undergo a division cycle that includes a surface attached mother cell that produces a planktonic swarmer cell upon division in order to extend the population to new ecological niches (29,30). The swarmer cell in the case of *C. crescentus* is non replicating and is out of the cell cycle (31). Our data support a similar role for the EB cell as the EB disseminates the infection, does not replicate and is out of the cell cycle (20).

The mother/swarmer cell developmental model fits our data for IB/EB production, but does not explain RB expansion. We have modeled this process (RB expansion to RB/IB asymmetric division) as maturation over time from an RB that produces two RBs thereby increasing the dividing cell population (RB_R), to a RB mother/stem cell (RB_E) that produces an IB through asymmetric division. Currently the mechanism for RB_R to RB_E maturation is unknown but could be influenced by a number of factors such as EB age at infection, time to nutrient acquisition in the cell, or through a yet to be described stochastic

maturation mechanism. Additionally, our data show that the expansion step produces significant heterogeneity in RB_E numbers in individual inclusions. This differential amplification is potentially a novel evolutionary adaptation to balance RB maturation and early EB production, i.e late maturation leads to late EB production but a high EB production rate, whereas early maturation leads to early EB production with a low EB production rate.

Overall, by using computational agent based modeling we have expanded the description of the developmental cycle. Our data support a four stage model, EB germination, RB amplification/maturation, IB production, and EB formation (Fig. 9). A key aspect of this model is the stochastic amplification and maturation of RBs (RB_R) from an expanding population to an stem cell RB population (RB_E) that produces IBs through asymmetric replication reminiscent of stalk/swarmer cell dynamics (Fig. 9). This is followed by an EB formation stage where the IB undergoes a dramatic phenotypic change that starts with the expression of the nucleoid associated protein HctA and ultimately ends with the expression of a second nucleoid associated protein HctB. This EB formation stage takes ~8 hours, ultimately resulting in the infectious EB (11) (Fig. 9.).

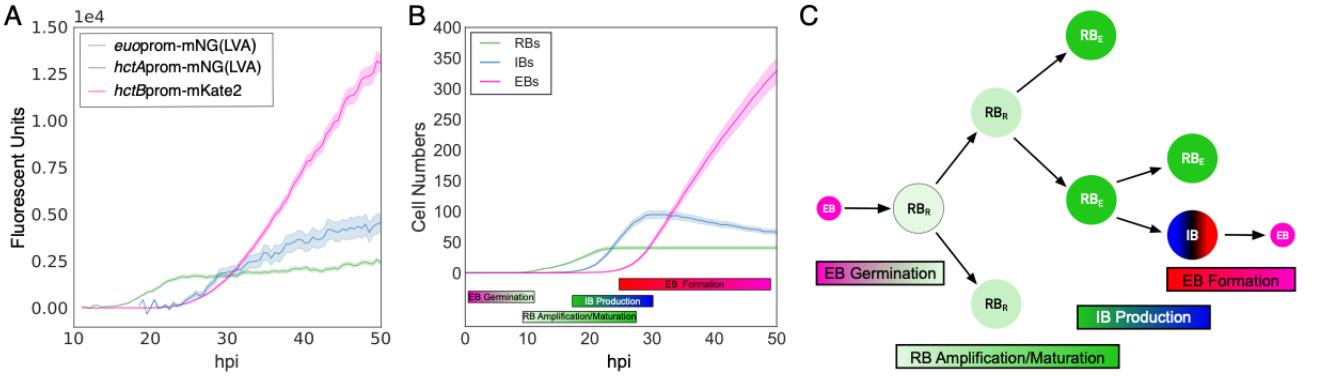

Figure. 9. Model of the developmental cycle. A. Cell-form specific live-cell kinetics from Figure 1. **B.** Simulated developmental cycle using the asymmetric division/maturation model. **C.** Schematic of the developmental model. Model consists of: EB to RB germination, RB amplification/maturation, asymmetric IB production, and direct IB to EB formation. RBs (*euo*): green; IB (*hctA*): blue>black>red; EB (*hctB*): pink.

Our experiments and models have focused on *Chlamydia* living in close to ideal growth conditions (11). It is likely that *Chlamydia* reacts and adapts the cycle to nutrient and other stresses. The creation

of an ABM that models the mechanisms of the developmental cycle under ideal conditions will provide a tool to help us visualize and understand the convolved data obtained from nutrient limiting, pharmacological, genetic, and molecular experiments. Ultimately, a better mechanistic understanding of the developmental cycle will lead to novel therapeutics targeting development as breaking the cycle will eliminate dissemination and chlamydial disease.

Materials and Methods

Organisms and cell culture. Cos-7 cells were obtained from (ATCC). Cells were maintained in a 5% CO2 incubator at 37°C in RPMI 1640 (Cellgro) supplemented with 10% fetal plex (FP) and 10mg/ml gentamicin. All *C. trachomatis* L2-bu434 (L2) strains were harvested from Cos-7 cells. Elementary bodies were purified by density centrifugation using 30% MD-76R at 48 hours post infection(32). Purified elementary bodies were stored at -80°C in sucrose-phosphate-glutamate buffer (SPG) (10 mM sodium phosphate [8 mM K 2HPO 4, 2 mM KH 2PO 4], 220 mM sucrose, 0.50 mM L-glutamic acid; pH 7.4). *Escherichia coli* ER2925 (*dam*$^{-}$/*dcm*$^{-}$) was utilized to produce unmethylated plasmids for transformation into *Chlamydia*.

Promoter reporter and inducible expression constructs. All constructs were created in the p2TK2SW2 plasmid background (33). Promoters and the *ftsI* ORF were amplified from *C. trachomatis*-L2 (LGV Bu434) genomic DNA using the indicated primers (**Table ST 4.1**). Fluorescent reporters were ordered as gBlocks and cloned using the In-fusion HD EcoDry Cloning kit (Takara). Promoter reporter constructs were created as previously described (11,34). The p2TK2SW2-E-*ftsI*3XFLAG was generated by replacing the *clover* gene with the *ftsI* ORF in the previously created p2TK2SW2-E-*clover*3XFLAG plasmid (13). Dual promoter reporter cassettes (*euo*prom-mNG(LVA)_*hctB*prom-mKate2 and *hctA*prom-mEos3.2_*hctB*prom-mKate2) were then inserted upstream of E-*ftsI*3XFLAG to produce the p2TK2SW2-E-*ftsI*3XFLAG_*euo*prom-mNG(LVA)_*hctB*prom-mKate2 and p2TK2SW2-E-*ftsI*3XFLAG_*hctA*prom-mEos3.2_*hctB*prom-mKate2 constructs.

Chlamydial transformation and isolation. Transformation of *C. trachomatis*-L2 was performed as previously described with selection using 500 ng/ul spectinomycin (33). Clonal isolation of transformants was achieved by inclusion isolation (MOI <1) via micro-manipulation. To confirm conality each construct was purified from the chlamydial transformants, transformed into *E. coli* and five colonies were sequenced.

Infections. Infections were synchronized by incubating Cos-7 cells with *C. trachomatis*-L2 EBs in Hank's balanced salt solution (HBSS) (Gibco) for 15 minutes at 37ºC while rocking. The inoculum was removed and cells were washed with prewarmed (37ºC) HBSS with 1 mg/ml heparin. The HBSS was replaced with fresh RPMI-1640 containing 10% FP, 10 µg/ml gentamicin, 1 µg/ml cycloheximide, and 1 mg/ml heparin sodium. Chlamydial cell division was inhibited by the addition of 0.5 µg/ml ciprofloxacin or 1 U/ml penicillin-G to the media. Expression of *ftsI*3XFLAG was induced by the addition of 0.5 mM theophylline to the media (13).

Replating assays. EBs were isolated from infected Cos-7 cells by scraping the host monolayer followed by centrifugation at 4ºC for 30 min at 18213 rcfs. EB pellets were resuspended in 4ºC RPMI via sonication and used to infect Cos-7 cells in polystyrene 96-well microplates in a 2-fold dilution series. Infected cells were incubated for 29 hours followed by methanol fixation. Fixed cells were stained with 4′,6-diamidino-2-phenylindole (DAPI) for visualization of host-cell nuclei and anti-MOMP antibody conjugated to FITC (Thermo Scientific™) for visualization of *Chlamydia*. Monolayers were imaged with an Andor Zyla sCMOS and Nikon Eclipse TE300 inverted microscope and the scopeLED illumination system at 470nm and 390nm, and BrightLine band pass emissions filters at 514/30nm and 434/17nm. Automated image acquisition was performed using µManager software (35). Inclusion numbers were quantified with custom scripts in ImageJ and analyzed in custom Python notebooks as previously described (11,32,34)

Genome number quantification. Total DNA was isolated from infected Cos-7 cells during active infections using an Invitrogen Purelink genomic DNA mini kit. A QX200 digital droplet system (BioRad)

was utilized for quantification of chlamydial genomic copies. A 2X ddPCR™ Supermix for Probes-No dUTP kit (BioRad) and a custom *copN*-specific primer/probe set was used for DNA detection (**Table ST 4.1**).

Live-cell microscopy. Monolayers were seeded on a multi-well glass-bottom plate and infected with *Ctr*-L2 EBs. Infections were grown in an OKOtouch CO2/heated stage incubator. Fluorescence images were acquired via epifluorescent microscopy using a Nikon Eclipse TE300 inverted microscope with a ScopeLED lamp at 470nm and 595nm, and BrightLine Bandpass filters at 514/30nm and 590/20nm. 20X/0.4NA dry, 40X/0.6NA dry, and 60X/1.40NA oil objective lenses were used. DIC was used to auto-focus images. Image acquisition was performed using an Andor Zyla sCMOS camera in conjugation with μManager software (35). Images were taken in 30 min intervals, unless otherwise stated. Imaging ranged from 10 to 60 hours after *Ctr*-L2 infection, depending on the experiment. Multiple fields were imaged for each treatment and the fluorescent intensity of individual inclusions was monitored using the Trackmate plug-in in ImageJ (15). Inclusion fluorescent intensities were averaged and graphed in Python as previously described (34)

Confocal microscopy. Cos-7 cells were seeded onto glass coverslips and infected with the appropriate *Ctr*-L2 strains. Samples were fixed at the designated times in 2% paraformaldehyde in phosphate-buffered saline (PBS) at room temperature, overnight. Samples were then washed with filtered PBS and stained with DAPI to visualize DNA and monoclonal anti-FLAG M2 antibody (Sigma, Thermo Scientific™) with alexa 647 anti-mouse secondary antibody to visualize FtsI3XFLAG expression. Coverslips were mounted onto a microscope slide using MOWIOL (100 mg/mL 150 MOWIOL® 4-88, 25% glycerol, 0.1 M Tris pH 8.5). Images were acquired using a Nikon spinning disk confocal inverted microscope with a 100X/1.45NA oil objective with a laser lamp at 405nm, 490nm, 568nm and 660nm. Image acquisition was performed using an Andor Ixon EMCCD camera and the Nikon elements software. Multiple inclusions were imaged for each treatment/time point and quantification of individual cells was performed using Trackmate. Chlamydial cell numbers were then analyzed in custom Python notebooks. Representative confocal micrographs are maximal intensity projections of 3D data sets.

Computational Modeling. Modeling was done using the CellModeller platform (16). The model description scripts and model data analysis scripts are described in supplemental information and available on github (SGrasshopper/Chlamydial-developmental-cycle).

Data Availability. All data, bacterial strains and methodologies are available upon request.

Funding: This work was supported by National Institutes of Health Grants R01AI130072, R21AI135691 and R21AI113617 (NG, SG). Additional support was provided by the Institute for Modeling Collaboration and Innovation (IMCI) Data Access Grant from the University of Idaho and pilot Grant (NIH COBRE P20GM104420).

References:

1. Mumtaz G, Sharara E, Dejong J, Sibai A, Roberts B, Abu-Raddad L. P800Prevalence of curable sexually transmitted infections among refugees: global systematic review and meta-analysis. In 2019.
2. States C on P and C of STI in the U, Practice B on PH and PH, Division H and M, Medicine NA of S Engineering, and, Vermund SH, Geller AB, et al. Sexually Transmitted Infections: Adopting a Sexual Health Paradigm. 2021.
3. Abdelrahman YM, Belland RJ. The chlamydial developmental cycle. FEMS microbiology reviews. 29(5):94959.
4. Clifton DR, Fields KA, Grieshaber SS, Dooley CA, Fischer ER, Mead DJ, et al. A chlamydial type III translocated protein is tyrosine-phosphorylated at the site of entry and associated with recruitment of actin. Proceedings of the National Academy of Sciences of the United States of America. 101(27):1016671.
5. Hackstadt T, Baehr W, Ying Y. Chlamydia trachomatis developmentally regulated protein is homologous to eukaryotic histone H1. Proceedings of the National Academy of Sciences of the United States of America. 1987;88(9):393741.
6. Kaul R. Eukaryotic-like histones in Chlamydia. Frontiers in Bioscience. 1995;
7. Belland RJ, Zhong G, Crane DD, Hogan D, Sturdevant D, Sharma J, et al. Genomic transcriptional profiling of the developmental cycle of Chlamydia trachomatis. Proceedings of the National Academy of Sciences of the United States of America. 100(14):847883.
8. Lee JK, Enciso GA, Boassa D, Chander CN, Lou TH, Pairawan SS, et al. Replication-dependent size reduction precedes differentiation in Chlamydia trachomatis. Nature Communications. 2016;9(1):45.
9. Rockey DD, Matsumoto A. The chlamydial developmental cycle. Prokaryotic Development. ASM Press, Washington D. C.; 2000. p. 40325.
10. Abdelrahman YM, Belland RJ. The chlamydial developmental cycle. Vol. 29, FEMS Microbiology Reviews. Oxford University Press; 2005. p. 94959.
11. Chiarelli TJ, Grieshaber NA, Omsland A, Remien CH, Grieshaber SS. Single-Inclusion Kinetics of Chlamydia trachomatis Development. Vol. 5, MSystems. American Society for Microbiology; 2020.
12. Clavel D, Gotthard G, Stetten D von, Sanctis DD, Pasquier H, Lambert GG, et al. Structural analysis of the bright monomeric yellow-green fluorescent protein mNeonGreen obtained by directed evolution. Vol. 72, Acta Crystallographica Section D Structural Biology. International Union of Crystallography; 2016. p. 1298307.
13. Grieshaber NA, Chiarelli TJ, Appa CR, Neiswanger G, Peretti K, Grieshaber SS. Translational gene expression control in Chlamydia trachomatis. Vol. 17, PLoS ONE. Public Library of Science; 2022.
14. Heppert JK, Dickinson DJ, Pani AM, Higgins CD, Steward A, Ahringer J, et al. Comparative assessment of fluorescent proteins for in vivo imaging in an animal model system. Vol. 27, Molecular Biology of the Cell. American Society for Cell Biology; 2016. p. 338594.
15. Tinevez J-Y, Perry N, Schindelin J, Hoopes GM, Reynolds GD, Laplantine E, et al. TrackMate: An open and extensible platform for single-particle tracking. Methods. 2015;115:8090.
16. Rudge TJ, Steiner PJ, Phillips A, Haseloff J. Computational modeling of synthetic microbial biofilms. Vol. 1, ACS Synthetic Biology. American Chemical Society (ACS); 2012. p. 34552.
17. Miyairi I, Mahdi OS, Ouellette SP, Belland RJ, Byrne GI. Different growth rates of Chlamydia trachomatis biovars reflect pathotype. The Journal of infectious diseases. 2006 Aug 1;194:3507.
18. Liechti G, Kuru E, Packiam M, Hsu Y-P, Tekkam S, Hall E, et al. Pathogenic Chlamydia Lack a Classical Sacculus but Synthesize a Narrow, Mid-cell Peptidoglycan Ring, Regulated by MreB, for Cell Division. PLoS pathogens. 2014;12(5):e1005590.

19. Heddle JG, Barnard FM, Wentzell LM, Maxwell A. The interaction of drugs with DNA gyrase: a model for the molecular basis of quinolone action. Vol. 19, Nucleosides, Nucleotides & Nucleic Acids. Taylor & Francis Group (Informa); 2000. p. 124964.
20. Grieshaber NA, Runac J, Turner S, Dean M, Appa C, Omsland A, et al. The sRNA Regulated Protein DdbA Is Involved in Development and Maintenance of the Chlamydia trachomatis EB Cell Form. Vol. 11, Frontiers in Cellular and Infection Microbiology. Frontiers Media S.A.; 2021.
21. Lambden PR, Pickett MA, Clarke IN. The effect of penicillin on Chlamydia trachomatis DNA replication. Microbiology (Reading, England). 2006 Sep 1;152:25738.
22. Hoare A, Timms P, Bavoil PM, Wilson DP. Spatial constraints within the chlamydial host cell inclusion predict interrupted development and persistence. BMC microbiology. 2006;8(1):5.
23. Omsland A, Sager J, Nair V, Sturdevant DE, Hackstadt T. Developmental stage-specific metabolic and transcriptional activity of Chlamydia trachomatis in an axenic medium. Proceedings of the National Academy of Sciences of the United States of America. 109(48):197815.
24. Abdelrahman Y, Ouellette SP, Belland RJ, Cox JV. Polarized Cell Division of Chlamydia trachomatis. PLoS pathogens. 2016 Aug 9;12(8):e1005822.
25. Gregory WW, Gardner M, Byrne GI, Moulder JW. Arrays of hemispheric surface projections on Chlamydia psittaci and Chlamydia trachomatis observed by scanning electron microscopy. Journal of bacteriology. 1979 Apr 1;138(1):2414.
26. Matsumoto A. Surface projections of Chlamydia psittaci elementary bodies as revealed by freeze-deep-etching. Vol. 151, Journal of Bacteriology. American Society for Microbiology; 1982. p. 10402.
27. Nans A, Saibil HR, Hayward RD. Pathogen-host reorganization during Chlamydia invasion revealed by cryo-electron tomography. Vol. 16, Cellular Microbiology. Hindawi Publishing Corporation; 2014. p. 145772.
28. Liechti GW, Kuru E, Hall E, Kalinda A, Brun YV, VanNieuwenhze M, et al. A new metabolic cell-wall labeling method reveals peptidoglycan in Chlamydia trachomatis. Vol. 506, Nature. Springer Nature; 2013. p. 50710.
29. Ausmees N, Jacobs-Wagner C. Spatial and temporal control of differentiation and cell cycle progression in Caulobacter crescentus. Annual review of microbiology. 2000;57:22547.
30. Lee K-C, Webb RI, Fuerst JA. The cell cycle of the planctomycete Gemmata obscuriglobus with respect to cell compartmentalization. BMC cell biology. 2009 Jan 14;10:4.
31. Skerker JM, Laub MT. Cell-cycle progression and the generation of asymmetry in Caulobacter crescentus. Vol. 2, Nature Reviews Microbiology. Springer Nature; 2004. p. 32537.
32. Grieshaber S, Grieshaber N, Yang H, Baxter B, Hackstadt T, Omsland A. Impact of Active Metabolism on Chlamydia trachomatis Elementary Body Transcript Profile and Infectivity. Vol. 200, Journal of Bacteriology. American Society for Microbiology; 2018.
33. Wang Y, Kahane S, Cutcliffe LT, Skilton RJ, Lambden PR, Clarke IN. Development of a transformation system for Chlamydia trachomatis: restoration of glycogen biosynthesis by acquisition of a plasmid shuttle vector. Vol. 7, PLoS Pathogens. Public Library of Science; 2011.
34. Chiarelli TJ, Grieshaber NA, Grieshaber SS. Live-Cell Forward Genetic Approach to Identify and Isolate Developmental Mutants in Chlamydia trachomatis. JoVE. MyJoVE Corp; 2020. p. e61365.
35. Edelstein AD, Tsuchida MA, Amodaj N, Pinkard H, Vale RD, Stuurman N. Advanced methods of microscope control using Manager software. Journal of biological methods. 2012;1(2):10.

Supplemental Information: Description of Agent-based Models

Model Description

Two agent-based models that simulate the developmental dynamics of *Chlamydia* at the single inclusion level were created using the Python-based platform Cellmodeller. Agent-based models simulate and track individual cells (agents) within large complex population structures. Cellmodeller is a framework that models cellular biophysics, gene regulation and intercellular signaling (1). Models are created within this framework using simple model definitions with Python. Cellmodeller tracks the properties of each cell during the simulations. For our models, the physical information (position, size), growth rates, and expression levels of HctA, HctB and Euo were tracked.

EB germination, RB amplification, IB conversion/production, and EB formation were simulated for both models. A germination time of 10 ± 2 hours was used, and a doubling time (*R*) of RBs was estimated to be ~2 ±.05 hours based on our kinetic experiments. The two models differ in the mechanisms that generate the IB cell type.

Creation of the IB

Direct Conversion model

In this model, RBs replicate symmetricity after germination to produce two RBs. Over time each new RB has an increasing chance of directly converting into an IB cell. We fit a sigmoidal function to the mean value of inclusion-level live-cell *euo*prom-mNG(LVA) expression data (Fig. 1). The function was set to scale between zero and one hundred percent and used to drive the percent chance of RB to IB conversion. Conversion was limited to a maximum of 50% chance of IB conversion as higher or lower values led to RB extinction or RB overproduction.

Asymmetric Production model

The asymmetric conversion model uses a maturation mechanism to switch from RB amplification to IB production. After germination, the initial RB (RB_R) divides symmetrically, producing two RBs after every division. The RB_R matures into the RB_E cell which acts as a stem cell producing an IB and regenerating the RB_E after every division. For this model we used the same sigmoidal function to drive RB_R to RB_E maturation.

RB conversion function and parameterization

As the mechanism that drives either RB amplification/maturation or direct conversion is still unknown, we fit the following sigmoidal function (1) to the mean value of inclusion-level live-cell *euo*prom-mNG(LVA) expression data using the optimize.curve_fit function from the SciPy package. The parameters for this function were adjusted to scale between zero and one hundred percent (Table 2) and used to drive the percent chance of RB_R to RB_E maturation (*M*) or chance of direct conversion for individual RBs (Figure 1).

$$M = \frac{L}{1 + e^{(m-(tR))c} + d}$$

Parameter	Value
m	2.15841312E+01
L	97.81
c	6.77630536E-01
d	2.19

Table 1: Parameters for RB maturation sigmoidal function.

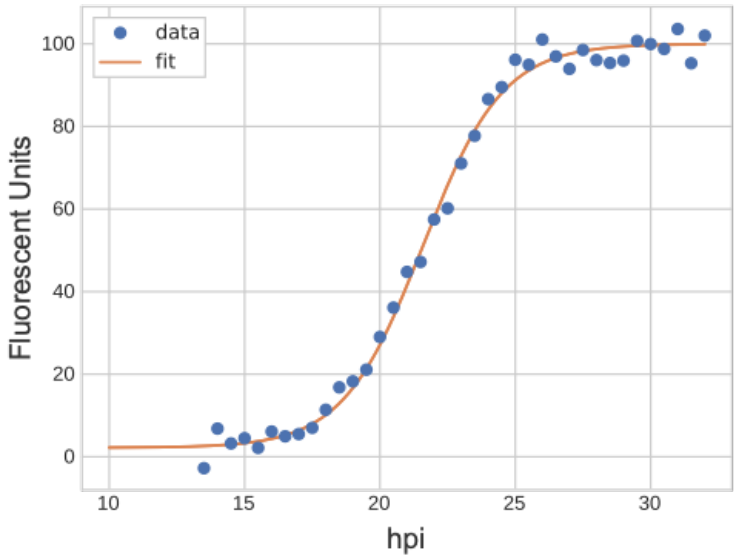

Figure 1: Sigmoidal function fit to live-cell *euo*prom-mNG(LVA) data. Inclusion-level data was collected from host cells infected with L2-BMELVA. Fluorescent intensity was collected every 15 min using automated live-cell microscopy. A sigmoidal function (orange line) was fit to the mean of the live-cell data from 10 to 32 hpi and then scaled from zero to one hundred percent.

Gene expression and EB formation

The models also simulate RNA transcription and protein production dynamics of Euo (E_R, E_P), HctA (A_R, A_P), and HctB (B_R, B_P) for each cell form. The kinetics and cell specificity for the expression of each of these proteins was based on our live-cell inclusion-level and single-cell data (**Fig. 1 and 2, main text**). For both models, RBs express Euo but not HctA or HctB. After IB formation the Euo production rate is set to zero and when Euo protein levels drop below a threshold due to degradation, HctA expression is de-repressed. When HctA protein concentration reaches a specified threshold, HctB expression is induced. Once HctB levels reach a specified concentration threshold the cell is considered an EB and infectious. The

following equations are used to drive RNA and protein expression in each cell form. The parameters for the equations are given in Table 2.

$$E_R = E_R + (pr_E R) - (nr_E E_R R)$$

$$E_P = E_P + (p_E E_P R) - (n_E E_P R)$$

$$A_R = A_R + (pr_A R) - (nr_A A_R R)$$

$$A_P = A_P + (p_A A_P R) - (n_A A_P R)$$

$$B_R = B_R + (pr_B R) - (nr_B B_R R)$$

$$B_P = B_P + (p_B B_P R) - (n_B B_P R)$$

Parameter	Description	Value
pr_E	*euo* RNA production rate	0.02
pr_A	*hctA* RNA production rate	0.04
pr_B	*hctB* RNA production rate	0.06
nr_E	*euo* RNA degradation rate	0.02
nr_A	*hctA* RNA degradation rate	0.01
nr_B	*hctB* RNA degradation rate	0.024
p_E	*euo* protein production rate	0.5
p_A	*hctA* protein production rate	1.0
p_B	*hctB* protein production rate	0.5
n_E	*euo* protein degradation rate	0.08
n_A	*hctA* protein degradation rate	0.05
n_B	*hctB* protein degradation rate	0.01

Table 2: Parameters used for expression dynamics.

Modeling cell division inhibition

To determine the effects of cell division inhibition on each cell type subpopulation, we simulated RB conversion to an alternative cell type where the RB was prevented in its ability to divide. For the direct conversion model, the RBs incapable of cell division were still permitted to convert directly into IBs based on the previously established rate of replication (conversion decision time equalling ~2 hours).

Modeling RB cell death

To determine the effects of RB cell death in both models the RBs were again classified as a separate cell type and removed from the RB population. However, this new cell type was inhibited in its ability of IB conversion/production regardless of the model.

The python model descriptions are available on GitHub at SGrasshopper/Chlamydial-developmental-cycle

References:

1. Rudge TJ, Steiner PJ, Phillips A, Haseloff J. Computational modeling of synthetic microbial biofilms. Vol. 1, ACS Synthetic Biology. American Chemical Society (ACS); 2012. p. 34552.

Supplemental figures:

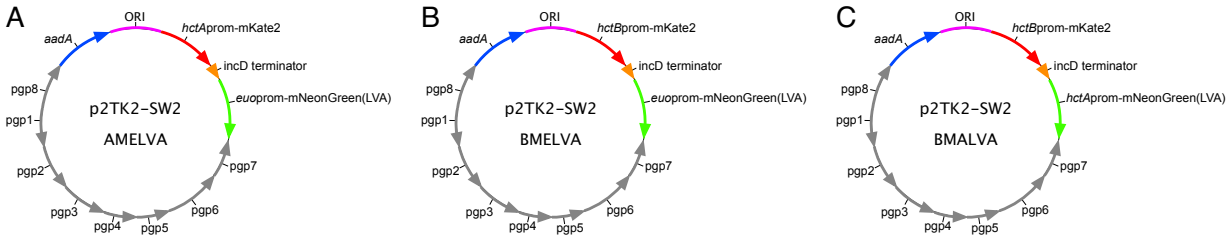

Figure S1: Schematic representation of the dual promoter reporter constructs. Promoter reporter cassettes were cloned into p2TK2SW2. Cassettes were inserted between the orfs of pgp7 and pgp8. A. p2TK2SW2-AMELVA encodes hctAprom-mKate2 and euoprom-mNeonGreen(LVA), B. p2TK2SW2-BMELVA: hctAprom-mKate2 and euoprom-mNeonGreen(LVA) and C. p2TK2SW2-BMALVA: hctBprom-mKate2 and hctAprom-mNeonGreen(LVA).

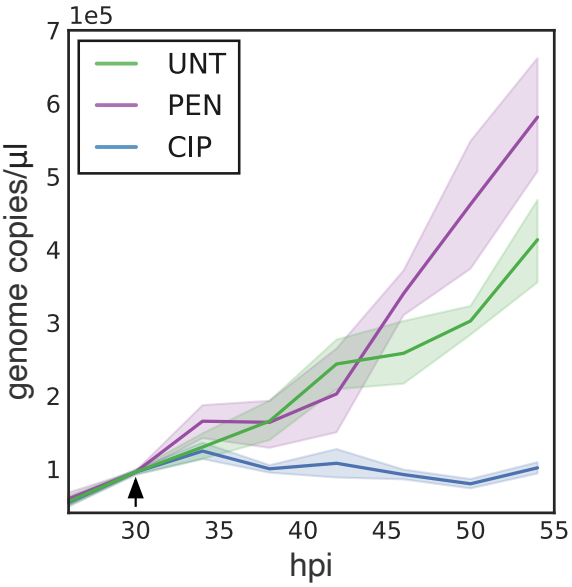

Figure S2: DNA replication is inhibited by ciprofloxacin treatment. Cos-7 cells were infected with L2-BMELVA EBs. Infected cells were treated at 30 hpi with vehicle-only (UNT): green, penicillin-G (PEN): purple, or ciprofloxacin (CIP): blue. Genome copies were quantified using ddPCR. Samples were harvested every 4 hours from 26-54 hpi. Arrow indicates treatment time. Means are shown. Cloud represents 95% ci.

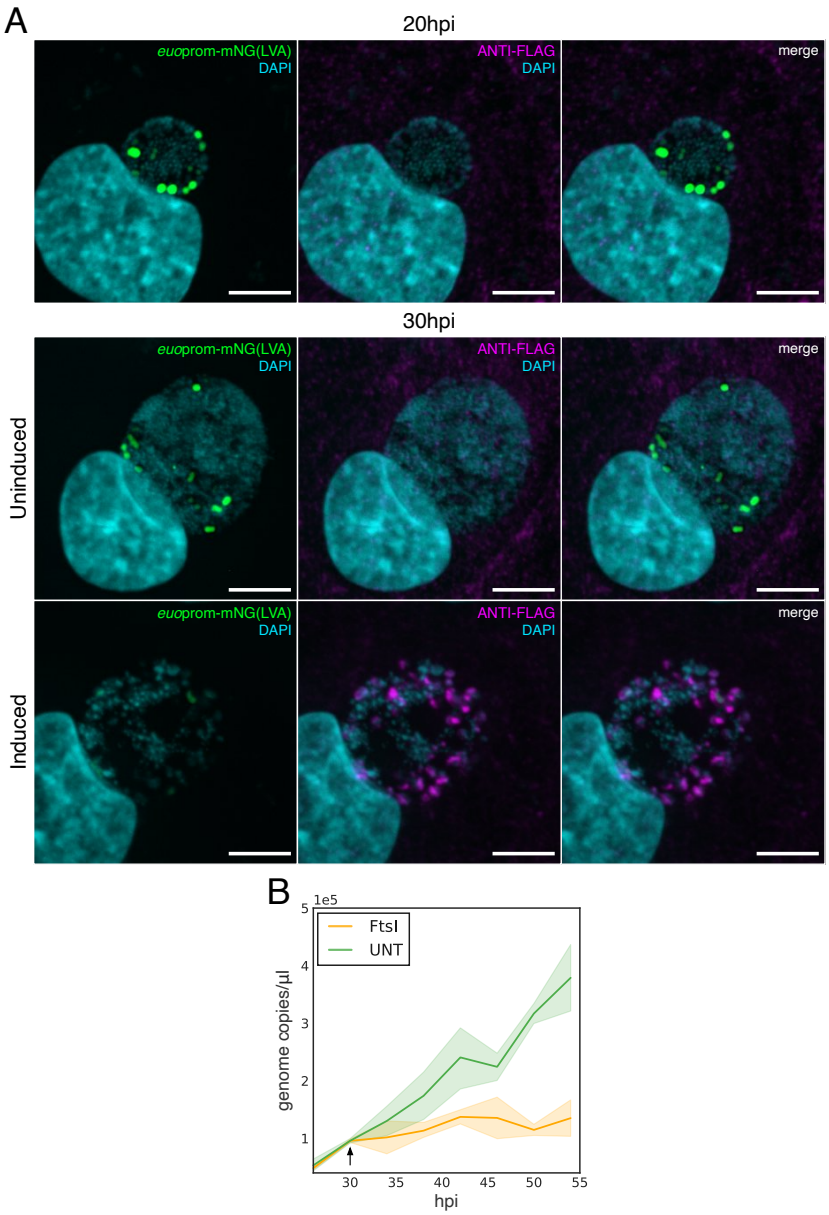

Figure S3: FtsI overexpression induces RB cell death. Cos-7 cells were infected with L2-E-ftsI3XFLAG-BMELVA. Infected cells were induced for FtsI3XFLAG expression at 20 hpi. A. Representative confocal micrographs of a 20 hpi infection and 30 hpi uninduced and induced infections. Samples were fixed at 20 hpi (pre-treatment) or 30 hpi, stained with DAPI and an anti-FLAG antibody for immunofluorescence (IF) imaging. euoprom-mNG(LVA): green, DAPI: cyan, anti-FLAG: magenta. Scale bar = 10 µm. B. Quantification of genome copies. Uninduced (UNT): green, induced (FtsI): orange. Samples were harvested every 4 hours from 26-54 hpi. Arrow indicates time of induction. Means are shown. Cloud represents 95% ci.

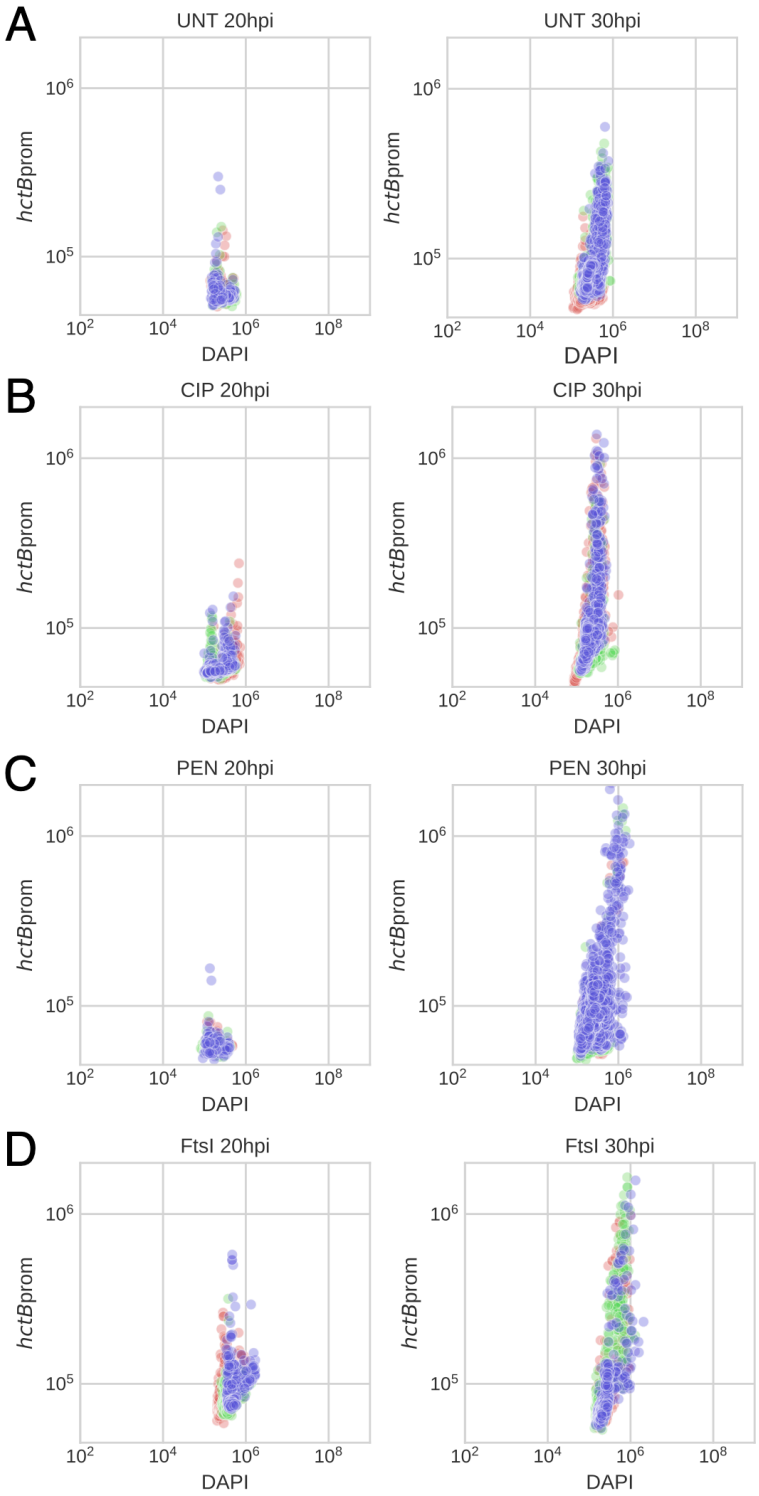

Figure S4: Single-cell quantification of EB production with cell replication inhibitors. Cos-7 cells were infected with L2-BMELVA (A-C) or L2-ftsI3XFLAG-BMELVA (D). Infected cells were treated with A: UNT, B: CIP, C: PEN, or D: induced for FtsI at 20 hpi. Cells were fixed and stained for DAPI at 20 and 30 hpi and imaged using confocal microscopy. Expression of DAPI and hctBprom-mKate2 was quantified on a single-cell basis using Trackmate from 3 individual inclusions per treatment per time point. Each color corresponds to chlamydial cells quantified within the same inclusion.

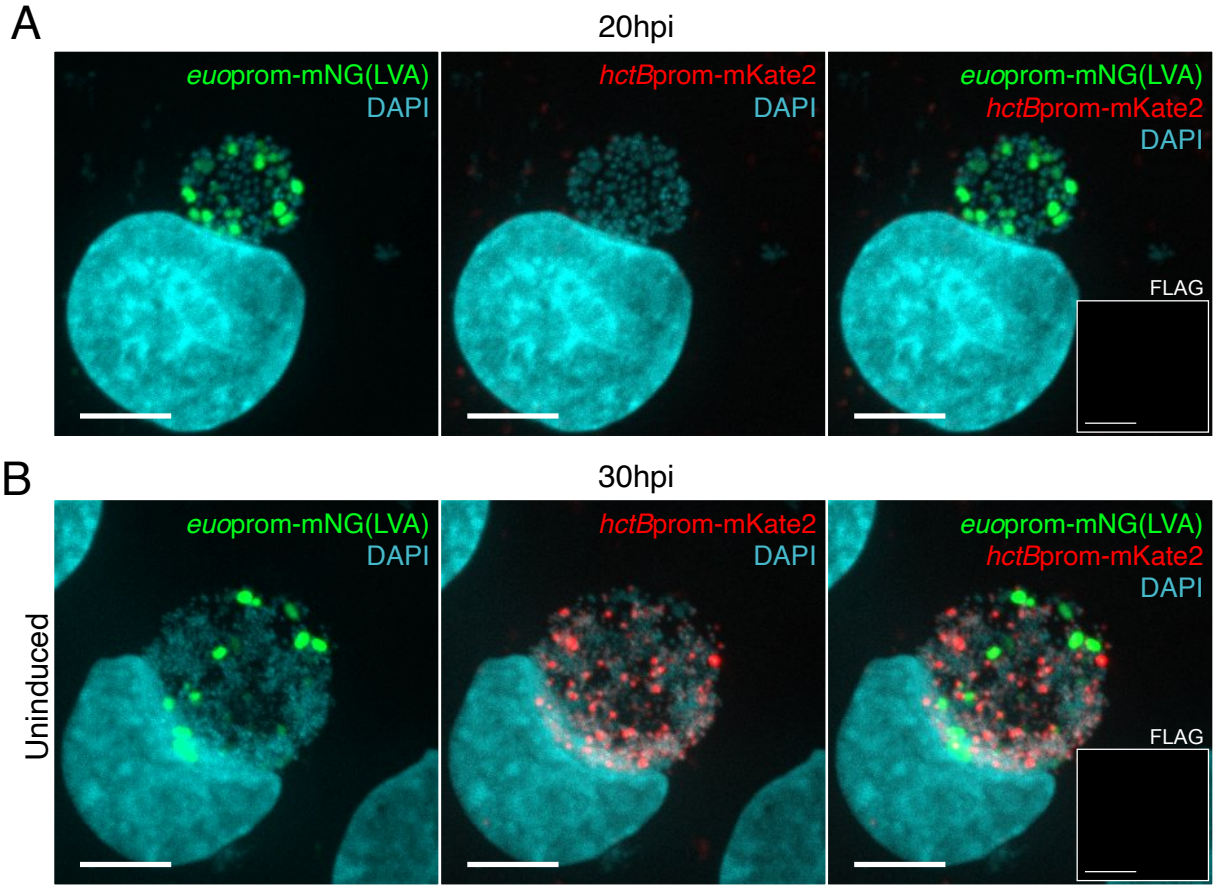

Figure S5: Confocal micrograph of uninduced L2-ftsI3XFLAG-BMELVA. Representative fixed confocal micrographs of Cos-7 cells infected with L2-ftsI3XFLAG-BMELVA at 20 hpi (A) and 30 hpi (B). Fixed samples were stained with DAPI and anti-FLAG. Insert demonstrates the lack of FLAG expression in both samples. Scale bar = 10 μm.

Movie S1: Single inclusion simulation of the Asymmetric Production model. Simulated individual cell-form development of a single inclusion. Germinating EB: lavender, RBs: green, IBs: blue>black>red, and EBs: pink. The green circle follows the progression of three RBs. Individual RBs persist throughout the cycle demonstrating stem cell-like properties.

Movie S2: Single inclusion simulation of the Direct Conversion model. Simulated individual cell-form development of a single inclusion. Germinating EB: lavender, RBs: green, IBs: blue>black>red, and EBs: pink. The green circle follows the progression of multiple individual RBs. Individual RBs are transient as they convert into IBs. However, RB division is matched with RB-to-IB conversion, leading to a fluctuating steady-state in RB numbers.

Movie S3: Live-cell time-lapse movie of RB stability throughout an active infection. Cos-7 cells were infected with L2-BMELVA. 40X automated live-cell fluorescence microscopy was used to monitor individual RBs (euoprom-mNG(LVA)+ cells) within single inclusions every 15 minutes from 24-60 hpi. The hctBprom-mKate2 promoter reporter was used for inclusion identification and to monitor inclusion development.

Movie S4: Live-cell time-lapse movie of transient IBs throughout an active infection. Cos-7 cells were infected with L2-BMALVA. Automated live-cell fluorescence microscopy was used to monitor individual IBs (hctAprom-mNG(LVA)+ cells) within single inclusions every 15 minutes from 24-60 hpi. The hctBprom-mKate2 promoter reporter was used for inclusion identification and to monitor inclusion development.